Aalto-yliopisto
Aalto-universitetet
Aalto University

Master’s Programme in Mechanical Engineering

# Residual Stress and Stress Corrosion Cracking of Austenitic Stainless Steels in Nuclear Environments

---

**Ahmed Mazhar**

**Master’s thesis**
**2024**

Aalto-yliopisto
Aalto-universitetet
Aalto University

**Author** Ahmed Mazhar
**Title of thesis** Residual Stress and Stress Corrosion Cracking of Austenitic Stainless Steels in Nuclear Environments
**Programme** Master's programme in Mechanical Engineering
**Major** Engineering Materials
**Thesis supervisor** Prof. Iikka Virkkunen
**Thesis advisor(s)** DSc. (Tech) Risto Ilola
**Date** 02.09.2024 **Number of pages** 73 **Language** English

## Abstract

This thesis investigates the potential role of thermal loads promoting stress corrosion cracking in welded type 316L SS austenitic stainless steels in the PWR environments. The representative weld sample of type 316L SS was manufactured from the PWR primary circuit piping segment. Local regions of the weld area were subjected to thermal loading to induce plastic strain and residual stresses. The thermally loaded samples were then exposed to PWR environment in the autoclaves at VTT for a period of one month. Optical and electron microscopic examination was carried out on the samples to observe potential cracks. Furthermore, EBSD analysis was carried out to observe any misorientations between the grains and crystallographic orientation of the weld and base metal. The results did not show any potential cracks in the samples indicating that SS316L can withstand thermal loads and residual stresses in corrosive environments without developing any cracks. Overall, the results demonstrated the susceptibility of type 316L SS and the effect of thermal loading and residual stresses on austenitic stainless steels when exposed to aggressive environments in the nuclear industry.

**Keywords** Stress corrosion cracking (SCC), austenitic stainless steels (ASS), residual stresses (RS), thermal cyclic loading, nuclear environments.

# Table of contents

## Acknowledgements

I want to thank Prof. Iikka Virkkunen and my thesis advisor Risto Ilola for their good advice and guidance. They guided me throughout my thesis journey here at Aalto University and helped me make this thesis a success.

I would like to pay special gratitude to Prof. Iikka Virkkunen for believing in me and choosing me to work for this crucial project. Without his support and guidance, this journey would not have been possible.

I am truly grateful to DSc. (Tech) Risto Ilola for his unwavering support and constant guidance during my thesis. He put commendable efforts from his side in helping me manage my practical work related to and guided me with his professional and technical expertise. Due to his guidance and support, I was able to perform my practical work without any obstacles in the laboratories.

I would like to thank my family and my partner who was there with me at each stage of this journey. She emphasized the importance of this thesis project and provided me with all the moral support and needed motivation during this period.

In the end, I would again like to thank each, and everyone involved with me in this thesis project, and I am really grateful with the bottom of my heart to all of you.

## List of figures

# List of tables

# Abbreviations

| | |
|---|---|
| SSC | Stress Corrosion Cracking |
| ASS | Austenitic Stainless Steel |
| PWR | Pressurized Water Reactor |
| BWR | Boiling Water Reactor |
| CT | Compact Tension |
| XRD | X-Ray Diffraction |
| NPP | Nuclear Power Plant |
| CW | Cold Worked |
| DT | Destructive Testing |
| NDT | Non Destructive Testing |
| CW | Cold Worked |
| SA | Solution Annealed |
| YS | Yield Strength |
| LWR | Light Water Reactor |
| FBR | Fast Breeder Reactor |
| TTP | Time Temperature Precipitation Phase |
| IASCC | Irradiation Assisted Stress Corrosion Cracking |
| SEM | Scanning Electron Microscopy |
| EBSD | Electron Backscattered Diffraction |

# 1 Introduction

Stress corrosion cracking (SCC) remains one of the most important piping degradation mechanisms that affects the plant lifetime management. SCC requires a susceptible material, the presence of tensile stresses and corrosive environment. SCC damage is apparent when the surface cracking propagates into the material. There have been numerous cases of SCC cracking in austenitic stainless steels in the Primary Water Reactor (PWR) environments in the nuclear industry [1], [2], [3] . These studies indicate that the problem has not yet been fully mitigated even with controlled water and alloy chemistry. It is necessary to understand the contributing factors that constitute such specific circumstances. Thermal loads may contribute to the promotion of SCC cracks in austenitic stainless steels when exposed to aggressive environment. The uneven plastic deformation that may be induced by thermal loads can lead to the formation of thermal residual stresses in steels which can be a major contributing factor in the formation of SCC cracks [4].

The purpose of this thesis is to understand the role of thermal loads as a contributing factor in promoting potential SCC in the PWR environments. The solution annealed type 316L SS samples are subjected to thermal loads and the focus area of thermal loads were on the welded part of the samples. The corresponding thermal residual stresses are measured and characterized using X-Ray diffraction. The thermally cyclic loaded samples are then exposed to simulated PWR environment in the autoclaves to study the incubation and development of SCC cracks. The samples are investigated for potential SCC cracking after exposure by destructive examination and the potential effects of induced thermal loads such as hardening and plastic strains on the material are studied.

## 1.1 Structure of the thesis

The rest of the thesis is structured as follows. Chapter two discusses the role and applications of austenitic stainless steels in nuclear applications. The formation and effect of residual stresses in austenitic stainless steels is discussed in chapter three of the thesis. Chapter four discusses the stress corrosion cracking in austenitic stainless steels in nuclear environments as well as the factors contributing to SCC when austenitic stainless steels are subjected to thermal cyclic loading. The experimental work on SS316L samples including the SCC test and SEM analysis is included in chapter five of the thesis. Chapter six discusses the results from the experimental work and short discussion of those results. Chapter seven includes the combined discussion of all the results from chapter six. The thesis concludes with the conclusion of this research in chapter eight.

# 2 Austenitic Stainless Steels in Nuclear Environments

Austenitic stainless steels (ASS) are widely used in nuclear power plants due to their excellent corrosion resistance and mechanical properties. Their common usage and applications are found in commercial boiling water reactor (BWR) and pressurized water reactor (PWR) systems as in-core and surrounding structural material. Typical commercial steel grades that are relevant and used in the nuclear reactor applications include type SS 304,316,321 and 347 stainless steels[5]. They have good strength and ductility at both high and low temperatures with excellent fatigue resistance and are most used in the solution annealed condition. In the solution annealed phase, the alloying elements are completely dissolved in the parent austenitic phase with little or no precipitation.

## 2.1 Properties of ASS for Nuclear Environment Applications

This section will discuss the factors that affects the properties of austenitic stainless steels in the nuclear reactor environments. There are both physical and mechanical properties of austenitic stainless steels that are critical for the nuclear applications.

### 2.1.1 Precipitation behavior during elevated temperature Aging

Austenitic stainless steels have very little or no delta ferrite in solution annealed condition, and it stays completely austenitic from room temperature up to 550°C. However, as the temperature increases above 550°C, austenitic stainless steels can start to experience the effects of thermal ageing decreasing the yield strength (YS) and ductility of the material. For typical light water reactors (LWR) or fusion reactor applications. This ageing behaviour is significant when considering the irradiation induced precipitation behaviour for fast breeder reactor (FBR) irradiation of components at temperatures of 400-750°C. Figure 1 shows the TTP curve for solution annealed 316 which is thermally aged at 550°C and above and it tends to produce precipitates along the grain boundaries. Cold work (CW) can also contribute to the formation of these precipitates even at lower temperatures. This various precipitate phase that are formed in 300 austenitic stainless steels during thermal aging with their nature and characteristics are also reported in [6], [7], [8].

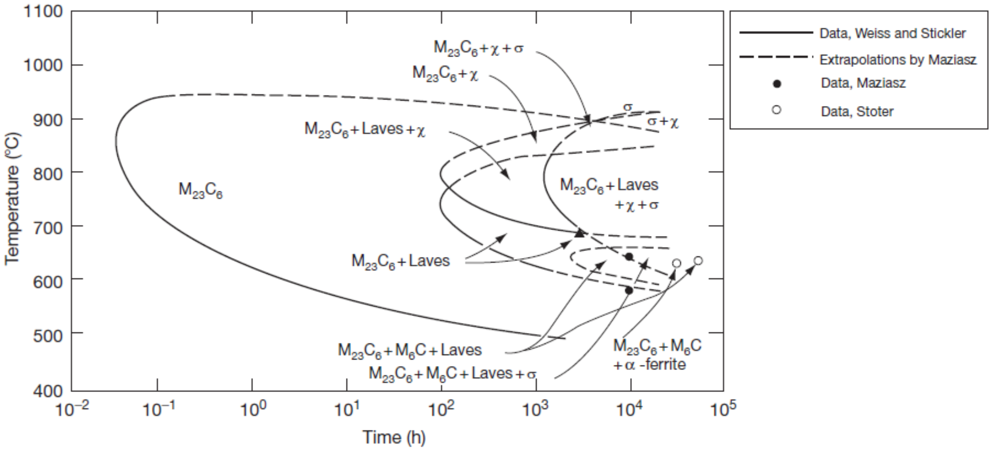

Figure 1 : Time-temperature precipitation phase (TTP) diagram for Solution Annealed 316 thermally aged[5].

### 2.1.2 Corrosion and Oxidation behavior

Austenitic stainless steels generally have good corrosion resistance to various types of acidic or other corrosive environments at room temperature and up to 200-300°C. Stresses in any form if present can contribute to the stress corrosion cracking (SCC) of these steels. The use of low carbon stainless steels such as type SS 304L and 316L can reduce to SCC. However, there is a major threat when austenitic stainless steels are exposed to supercritical water used in the nuclear reactors at or above 300°C. This exposure can cause severe corrosion damage and oxidation of austenitic stainless steels[9].

Fission or fusion reactor neutron irradiation can affect the properties of austenitic stainless steels in light water reactors (LWR). The major effects of irradiation on the mechanical properties of stainless steels are the increase in hardness (increased YS) and reduced ductility in solution annealed 316 stainless steels. This increased hardening and reduced ductility can further intensify if the steels are 20-25% cold worked. Figure 2 illustrates the increased yield strength for irradiated stainless steels[10]. The solution annealed stainless steels have 250-300 MPa yield strength in the irradiation condition, However, the irradiation increases the yield strength up to 600-800MPa and the ductility is reduced by 10% or less. This irradiation induced hardening is caused by the microstructural changes in the low temperature regime.

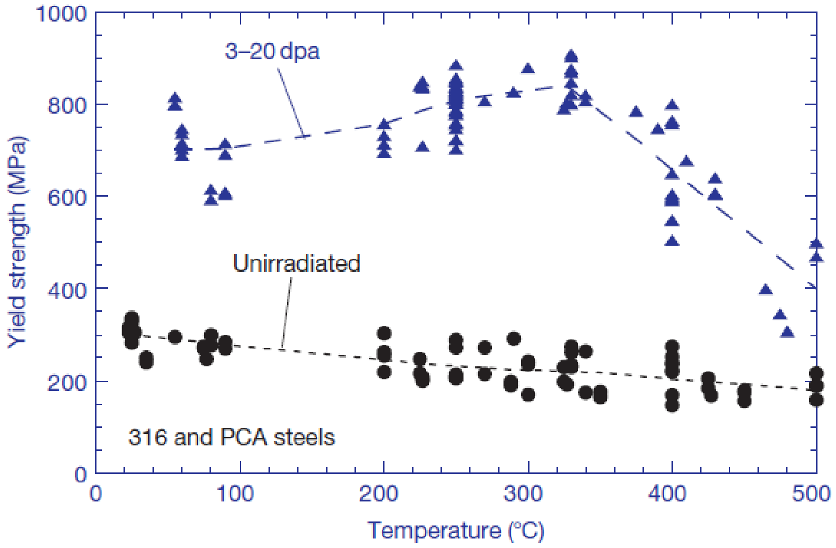

Figure 2 : Yield strength as a function of irradiation temperature for SA 316 and PCA in various reactors [5].

### 2.1.3 Mechanical Properties

The irradiation from the nuclear reactor also effects the mechanical properties of the austenitic stainless steels. The tensile properties of austenitic stainless steels that are irradiated at 300°C or above reflect the microstructural changes and specially the dislocation component of the microstructure. This higher temperature regime in austenitic stainless steels is marked by higher temperatures and dependencies of all the microstructural and precipitation changes[8], [11]. The yield strength decreases from 800MPa values at 300°C to about 400MPa at 500°C which is equal to the yield strength of unirradiated steels. This happens due to the coarsening of the radiation induced microstructure and the decrease of dislocation density by several magnitudes. Ductility is affected but not as much as it remains higher (>10%) at 400-500°C. The variation in the mechanical properties also depends on the type of reactors that are being used. Additionally, the irradiation can also have a significant effect on the grain boundary sensitization of austenitic stainless steels. Inazumi et al.[12] conducted the electrochemical testing of cold worked 316 stainless steels irradiated in Oak Ridge Research Reactor (ORR) at 330 and 400°C to detect the grain boundary sensitization. The sensitization phenomena were observed due to lower chromium at the grain boundaries. In light water reactor (LWR) systems, there have been concerns about irradiation assisted stress corrosion cracking (IASCC) at 300°C which are important for the extended service of the reactors[13].

## 2.2 ASS Components in BWR and PWR Environments

Austenitic stainless steels are used as a construction material for both BWR and PWR components. In BWR, austenitic stainless steels are used for piping and structures inside the pressure vessels. They are also used for components such as pumps, valves, sleeves and in auxiliary systems such as water tanks.

For PWR systems, austenitic stainless steels are used in steam generators where the tubes are made of Ti stabilized stainless steels. Most steam generator tubes in western PWRs are made of nickel-based material, that is alloy 690, while a smaller number of steam generators are made of iron-based alloy 800. Both the steam generator vessel and the pressurizer are clad with austenitic stainless steel[14].

# 3 Residual Stresses in Austenitic Stainless Steels

The residual stresses are defined as those stresses which remain in the material even after the removal of external forces[15] .Residual stresses in austenitic stainless steels can be formed due to several factors which include manufacturing processes, thermal gradients, heat treatment conditions and other factors. It is essential to determine the mechanism of the formation of residual stresses in austenitic stainless steels and the behaviour of these steels during service in different environments and applications. This chapter will focus on describing the residual stress formation mechanism and consequently their effects on the mechanical properties of austenitic stainless steels.

## 3.1 Mechanisms and Formation of Residual Stresses

As discussed under the main heading of this chapter, residual stresses are formed in austenitic stainless steels due to different manufacturing processes of which one of the most common processes is welding. The welding of austenitic stainless steels can induce residual stresses into the material, and it is necessary to know the mechanism of formation of these stresses.

During the welding thermal cycle, the variation in the temperature induces macroscopic elastic plastic distortions, which can result in number of macroscopic deformations [2]. These deformations can have an adverse effect on the overall welding performance and can lead to the formation of residual stresses.

Figure 3 illustrates the three main origins of the formation of residual stresses in welds, namely, mechanical, thermal, and metallurgical.

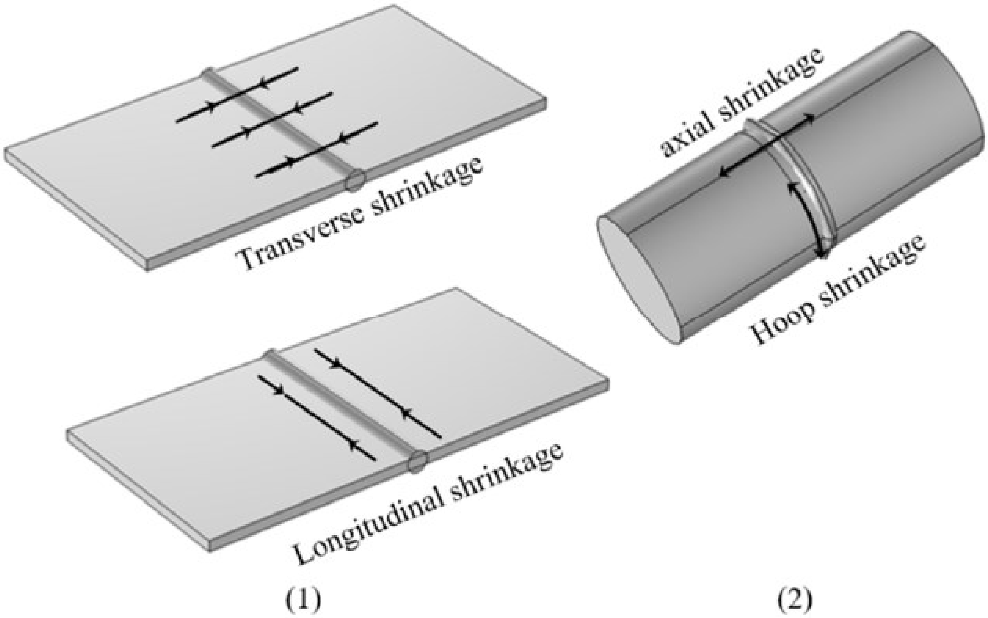

Figure 3 : Elementary effects of welding for (1) welded plates (2) Welded cylinders [15] .

## 3.2 Factors Influencing Residual Stresses

### 3.2.1 Welding Parameters

There are number of factors that can contribute to the formation of residual stresses in welded components. The effect of welding conditions/parameters on the formation of residual stresses has been studied by Teng and Lin [16]. The effect of specimen thickness, travel speed and preheating on the residual stresses of the welded joint were discussed and reported. According to the literature, the residual stresses increased with the decreasing thickness of the specimen. A higher welding speed results in lower residual stresses. Furthermore, preheating generally influences the formation of residual stresses of the welded joints and therefore it is necessary to implement the preheat treatments which helps in reducing the cooling rates and therefore results in reducing the residual stresses as well.

The condensation of heat in the welding region both inside and outside the weld zone results in uneven heating and cooling cycles therefore resulting in diverse plastic deformation within the weld zone and that results in the formation of residual stresses. Some authors have reported the use of 2D and 3D numerical models to predict the temperature distribution and residual stress in the welds and then comparing them with the experimental results

[17],[18],[19]. From the past studies, it was observed that the 3D models provide more reliable results than the 2D ones specially in the circumferential butt welding of pipes. Asadi et al.[20] studied a 3D Finite element model using the ABAQUS software to simulate the circumferential TIG welding of SS 304 stainless steel pipes. The effects of weld pass numbers, electrode moving speed and heat input were investigated. The simulation result showed that tensile residual stresses decrease on increasing the welding speed. Additionally, it was also reported that three pass welding process is more effective in producing fewer residual stresses than the two pass welding.

### 3.2.2 Mechanical / Thermal Loading

Thermal and mechanical residual stresses often exist in a component. These residual stresses are a result of uneven yielding during manufacturing operations or due to thermal treatments[4]. Residual stresses can also be found in components due to plastic deformation (strain induced martensitic deformation). Two phase materials such as duplex stainless steels may develop micro stresses due to the differences in the thermal and mechanical properties between the two phases. Moverare.J[21] studied the changes in the plastic deformation of duplex stainless steels resulting in the residual micro stresses. These residual stresses were also the result of complex load partitioning between the two phases because the hot and the cold rolled duplex stainless steel exhibits anisotropic material properties. The effect and the evolution of micro residual stresses during cyclic loading was studied by X-ray diffraction. A similar study was carried out by Johansson et al. [22] where they studied the evolution of micro and macro stresses in a duplex stainless steel during loading. Due to the differences in the coefficient of thermal expansion between the two phases of duplex stainless steels, compressive residual stresses were found in the ferritic phase whereas tensile residual micro stresses were found in the austenitic phase.

## 3.3 Measurement Techniques and Analysis Methods

There are several techniques and methods present in the literature that have been used to measure the residual stresses in welded joints of austenitic stainless steels. These methods include both destructive (DT) and non-destructive (NDT) mode of examination of residual stresses. This section will cover some of the commonly used techniques for measuring the residual stresses in austenitic stainless steels.

### 3.3.1 X Ray Diffraction (XRD) Method

#### 3.3.1.1 Principal of X-Ray Diffraction

X Ray Diffraction or the XRD method is one of the advanced nondestructive methods that is used to measure residual stresses in austenitic stainless steels and is used by a wide range of industries.

When a crystal is bombarded with x-rays of a fixed wavelength, and at incident angles, intense reflected x-rays are produced when the wavelengths of the scattered x-rays interfere constructively. For the waves to interfere constructively, the differences in travel path must be equal to the integer multiples of the wavelength. When this constructive interference occurs, a diffracted beam of x rays will leave the crystal at an angle equal to that of the incident beam[23].

Figure 4 illustrates the Bragg's law for x ray diffraction .The interaction of the distance between the atomic planes, the incoming wavelength, and the angle at which the peak is diffracting is described by equation 1:

$$n\,\lambda = 2d\,\sin\theta \qquad (1)$$

where n (an integer) is the order of reflection, $\lambda$ is the wavelength of the incident x-rays, d is the interplanar spacing of the crystal and $\vartheta$ is the angle of incidence.

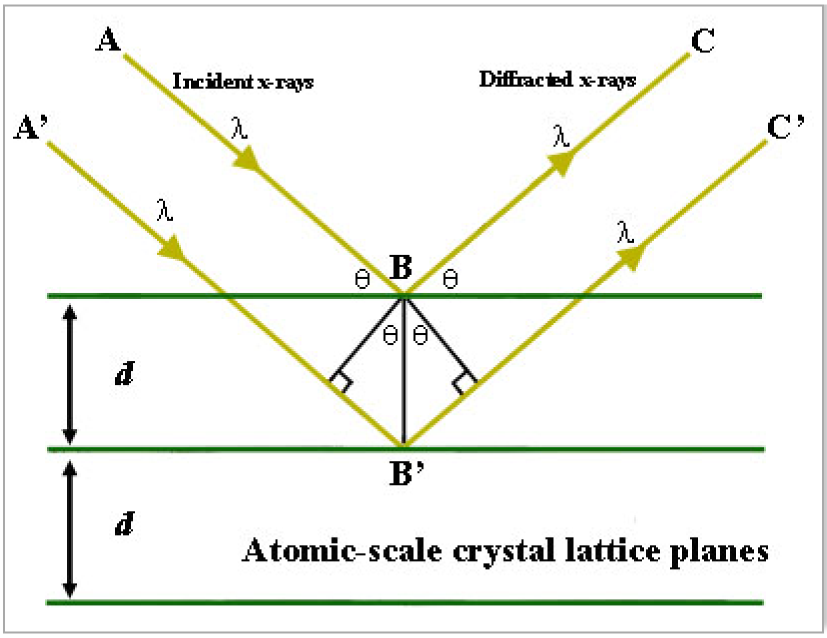

Figure 4 : Bragg's law reflection. The diffracted x-rays exhibit constructive interference when the difference between the paths ABC and A'B'C' differs by an integral number of wavelength (λ) [23]

#### 3.3.1.2 X-Ray residual stress measurement based on Fourier Analysis

Among the different X-ray measurement methods, the cos$\alpha$ method measures the stresses with single X-ray radiation. This allows shorter measurement time and simpler measurement system as compared to when the measurements are done with the conventional $sin\psi_0$ method. There have been several studies that have performed the X-ray measurement studies in cold rolled austenitic stainless steels using the $sin\psi_0$method [24][25]. The two-dimensional X-ray diffraction technique is reported using the cos$\alpha$ method in carbon steel where a four-point bend test was performed to measure the effectiveness of the proposed technique and to determine the Fourier series of Debye-Scherrer rings. The stresses obtained from the Fourier series were consistent with those determined using the cos$\alpha$ technique [26]. Since, this technique was successfully applied and tested for carbon steels, this new technique using the cos$\alpha$ method was also applied to austenitic stainless steels that are used in the nuclear industry [27]. The cos$\alpha$ method enables the measurements using single X ray irradiation thus reducing the total time of measurements and simpler measurement system compared to the conventional sin$\psi_0$ method. Figure 5 shows the stress measurement arrangement for XRD measurement while figure 6 displays the schematic of the XRD setup. In the figure, $\psi_0$ is the angle between the specimen surface normal and the incident angle of X ray.

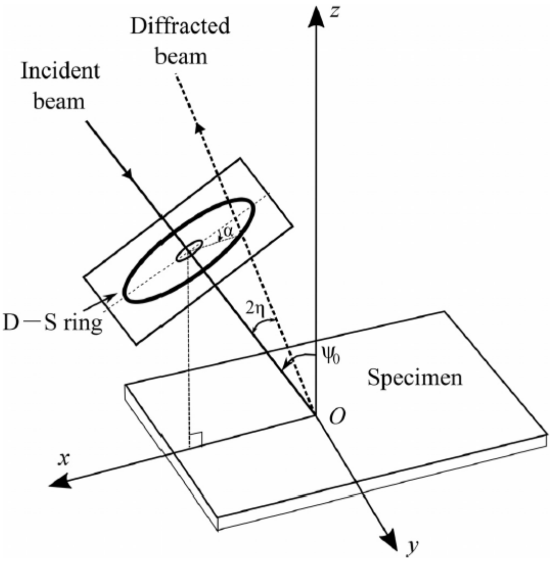

Figure 5 : Arrangement of specimen , X-ray, and IP [27]

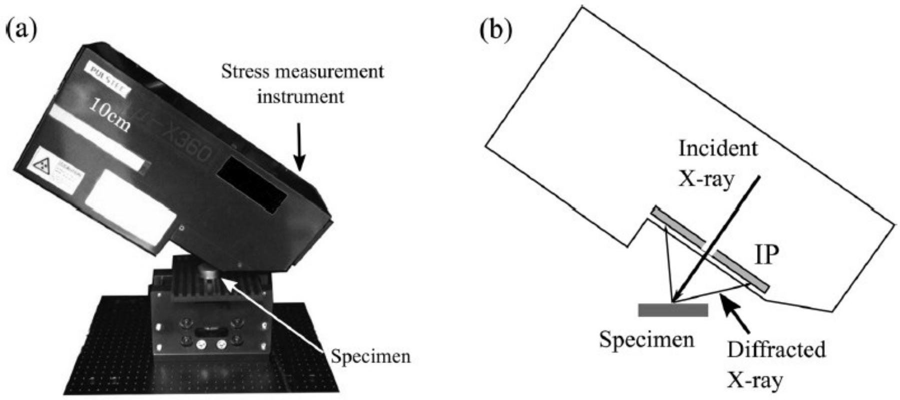

Figure 6 : Setup of the experiment. Distances from the specimen to IP were 35 and 32 mm for the Mn and Cr-X ray tubes respectively. (b) A simplified schematic of the setup [27]

Deng et al. [28] measured the residual stresses after deformation and analysed the stresses by XRD method by conducting uniaxial tensile tests of AISI SS304 specimens at different strain rates and temperatures. Figure 7 shows the residual stress behaviour at different loading positions. As the loading force increased, the value of residual stresses at the two positions (U1 and U2) also increased. Furthermore, the residual stress at position U1 was always higher than position U2 because it is close to fracture. When the specimens were measured under different degree of deformations, similar observations were reported.

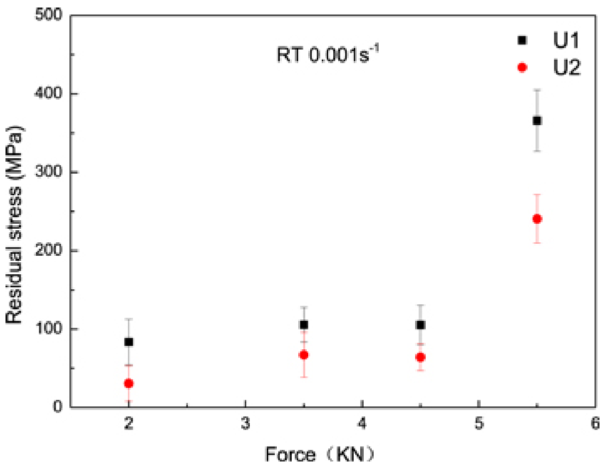

Figure 7 : Residual stress under different loading conditions [28]

### 3.3.2 Contour Method

The contour method is one of the most common methods used for measuring the residual stresses in steels. In this method, the part is cut into two pieces resulting in the redistribution of residual stresses which leads to deformation [29]. The shape (i-e contour) of the cut surface is measured and the data is used to compute the initial residual stress state.

There have been several studies that have used the contour method to measure the residual stresses. Mathew et.al[30] investigated the through thickness residual stresses in austenitic steel grith welded pipes using the contour technique. Hoop and axial residual stresses were measured on 300 series stainless steel material. The cutting method used was wire EDM. After cutting, the surface profiles were measured using a CMM machine. The 3D model of the cut pipe surfaces was created using ABAQUS Finite element model based on the measured parameters of the cut faces. The stress distribution on the top and bottom cut faces of each pipe was almost symmetrical which proved the effectiveness of the contour technique used. The results demonstrated that contour method is suitable for measuring the hoop and axial residual stresses in thick section pipe grith welds.

In another study, Yonezawa et al. [31] measured the residual stresses in cold worked type 316 stainless steel which were in compact tension(CT) state and were supposed to be used in simulated PWR primary water environment. Figure 8 shows the picture of CT coupons used and the diagram showing the coupon dimensions whereas Figure 9 shows the contour method principle. After cutting the specimen with wire EDM, the surface height profiles were measured with a laser scanning profilometer normal to the cut plane for each of the two opposing cut surfaces. The residual stress release on each measurement plane was determined by applying the negative of the smoothed surface profile as a set of displacement boundary conditions to cut the face of the linear elastic finite element model of the cut part.

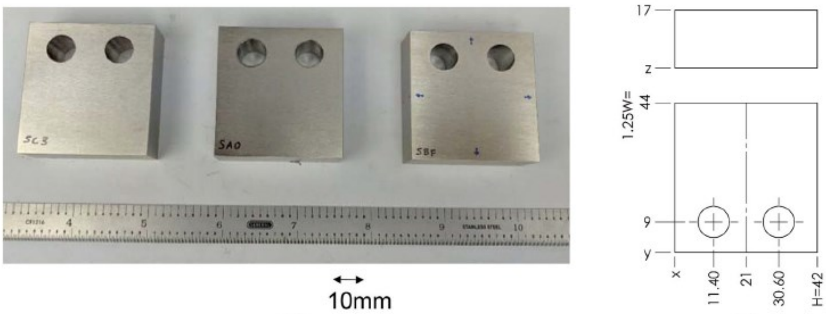

(a) (b)

Figure 8 : Photo of the CT coupons and (b) diagram showing the CT coupon dimensions [31].

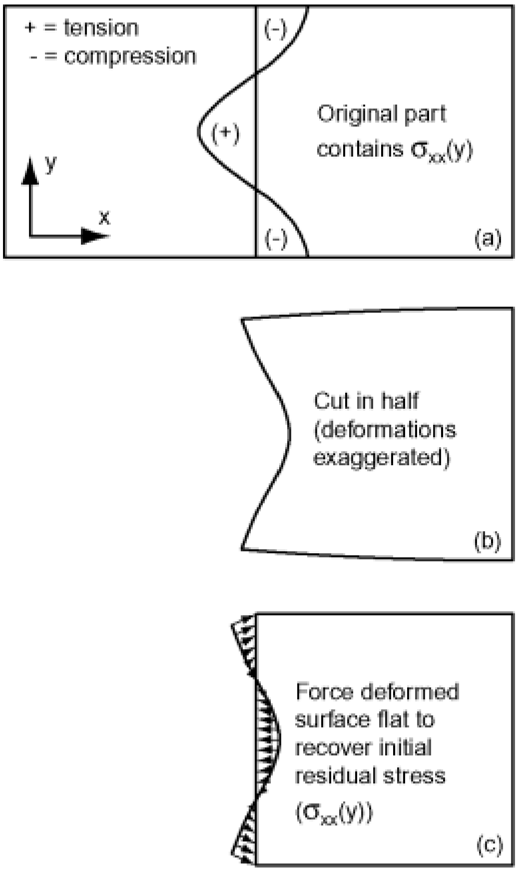

Figure 9 : Contour method principle (a) a body containing unknown residual stress is cut in half (b) the free surface deforms as stresses are released (c) applying the opposite of the deformations back to the part recovers the initial residual stress [29].

M.Turski and L.Edwards [32] reported the transverse residual stress measurements arise from single weld bead in an austenitic stainless steel plate using the contour technique. Figure 10 shows the nominal dimensions of the weld bead-on plate specimen. The specimen was cut using the same wire EDM method and then measured via CMM. In this study, after the measurement of the surface contour the cut surface was polished and etched to produce a micrograph showing the fusion boundary of the weld bead. Figure 11 shows the macrograph of the bead-on-plate specimen.

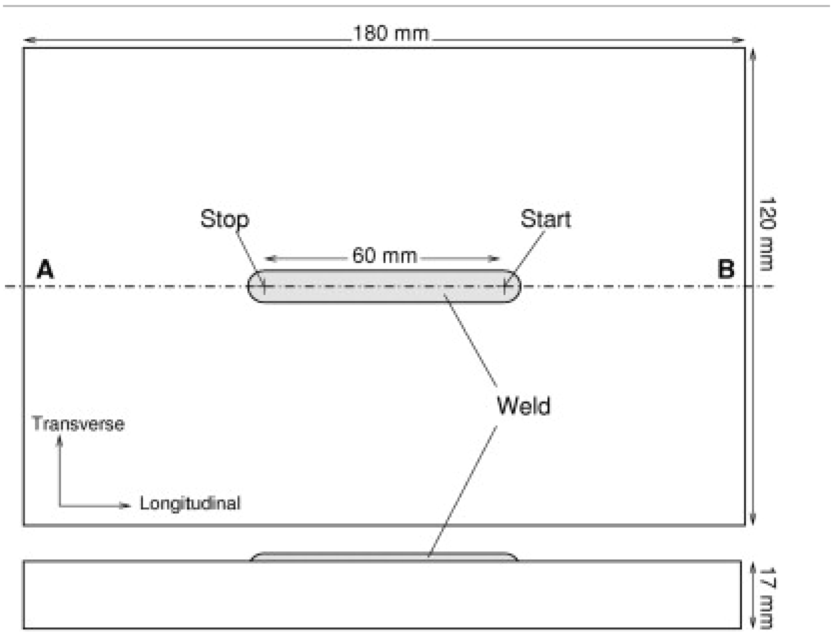

Figure 10 : Nominal dimensions of bead on plate specimen [32]

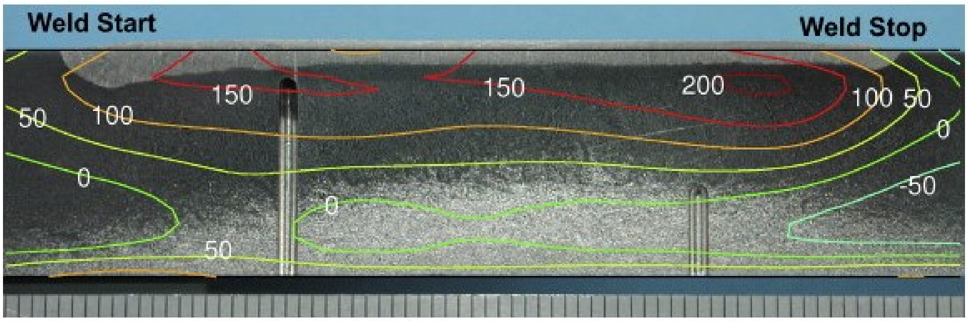

Figure 11 : Contour method transverse residual stress map overlaid on a macrograph of the bead-on-plate specimen [32].

### 3.3.3 Slitting Method

The slitting method is another destructive technique used for measuring the residual stresses in materials. It involves cutting through the specimen incrementally along the plane of interest. The change in the strain because of cutting is measured as a function of depth at locations along the cut surface. Several names have been used in the literature for the slitting technique such as crack compliance method, fracture mechanics approach, successive cracking method[33][34].

Hosseinzadeh et al.[35] studied the residual stresses using the slitting technique in an edge welded stainless steel beam. Figure 12 shows the schematic of the edge welded beam indicating the locations of the cut and the back face strain gauge. The centreline of the gauge was at the mi length of the sample. The specimen was cut using wire EDM. Stress data was gathered at specific increment of depth ranging from 0.1mm near the weld crown to 1mm deep within the beam. Figure 13 represents the measured strains as a function of cut depth. The graph shows that the strain increases with the cut depth increase.

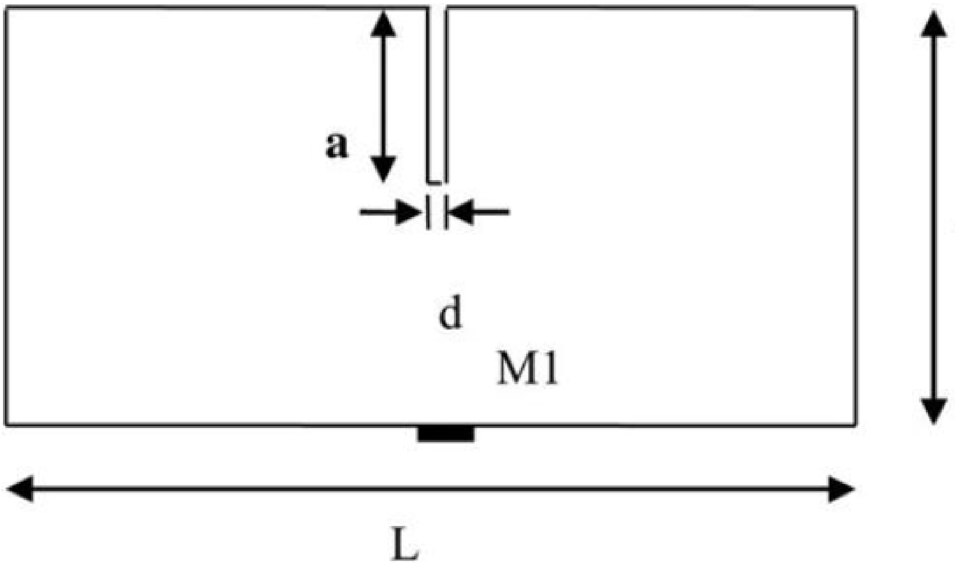

Figure 12 : Schematic diagram of the edge welded beam for the slitting method showing the cut off length of depth and location, M1, of the midthickness back face strain gauge that was aligned with the plane of the slit[29]

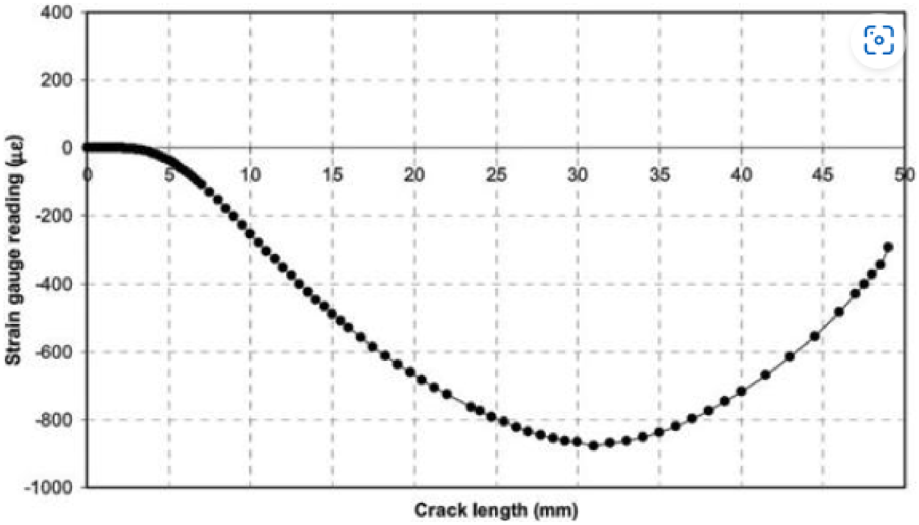

Figure 13 : Distribution of measured back-face strain against cut depth [35]

Olson et al. [36] in a study reported the residual stress measurements using the slitting technique in thin slices of pressurizer relief nozzle which is a cylindrical welded component in a nuclear power pressurized water reactor (PWR). He then compared the results obtained from slitting method to hole drilling and neutron diffraction methods. In another study by Mahmoudi et al[37], the stress variations along the line of cut during the slitting method is reported. Residual stresses of quenched samples of 316L were measured using the slitting technique. It was observed that the non-uniformity of the stresses in transverse direction along the cut plane could significantly affect the residual stress measurements. The study also compared the experimental results with those obtained from finite element simulations.

### 3.3.4 Hole Drilling Method

The hole drilling method is one of the destructive methods of measuring the residual stresses in a material. It is one of the most popular and widely used technique. The hole drilling method involves drilling a small hole into the specimen. This causes localized stresses and stain relaxations around the hole location and therefore it is necessary to select the correct experimental technique for hole drilling to avoid additional localized stresses particularly in strain hardening materials [38]. The strain relaxation is measured using a strain gauge rosette. Figure 14 shows the principle of the hole drilling method along with the ring core method which can be considered as an internalized variant of the hole drilling method[39].

However, for measuring of the non-uniform residual stresses, in which the stresses are varying with the depth of the hole surface, the conventional methods are not suitable as there are some shortcomings with the traditional methods. For this reason, advanced methods have been developed that can measure the non-uniform residual stresses in the material. Soete[40] in 1950 made a significant development to the hole drilling method by incorporating strain gauges enhancing the accuracy and reliability of stress measurement. This method was called the incremental strain method. There have been other studies that have reported the experimental work on the incremental strain method [41][42]. The other traditional method developed was the Average strain method. However, for the measurement of non-uniform in depth residual stresses, this method also proved to be inaccurate with certain shortcomings which have been recently identified[43][44],[45].

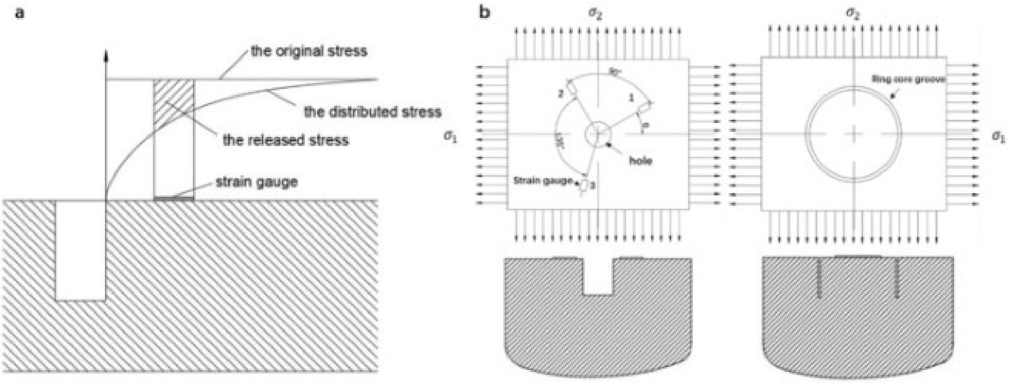

Figure 14 : Schematic diagram of (a) the hole drilling method and (b) the stress-release geometries of the hole drilling and ring-core methods [39] .

The finite element analysis of the calibration data provides better ways of measuring the non-uniform stresses in the material from incremental relaxed strain data. The integral method [46],[44][47] rely on the calculated calibration data and it covers the theoretical shortcomings which have been found in the traditional strain gauge methods.

# 4 Stress Corrosion Cracking in Austenitic Stainless Steels in Nuclear Environments

## 4.1 Mechanism of SCC

Stress corrosion cracking remains one of the most significant piping damage mechanisms that affect the plant lifetime management in nuclear power plants. SCC damage manifests a surface cracking that propagates into the material and can only be detected after crack incubation. austenitic stainless steels are commonly used in nuclear power plants environments, but they are susceptible to both intergranular and transgranular cracking. Improved water chemistry and increased chromium content in newer nickel based weld alloys has been thought to mitigate SCC problems in modern PWR designs and inlay repairs of susceptible weld alloys. SCC requires a susceptible material, the presence of tensile stresses and a corrosive environment. Figure 15 shows the circular loop which makes the conditions for potential SSC in materials. Intergranular stress corrosion cracking (IGSCC) has been a common mode of failure in BWRs while it has not been a common failure mode in PWRs under normal operating conditions [14]. This is because of the differences in the water chemistry of these two reactor types. However, the number of cases in PWRs experiencing IGSCC has been increasing over the years indicating that PWRs are not immune to IGSCC, and this failure mode must be considered in the plant life management strategies for PWRs as well.

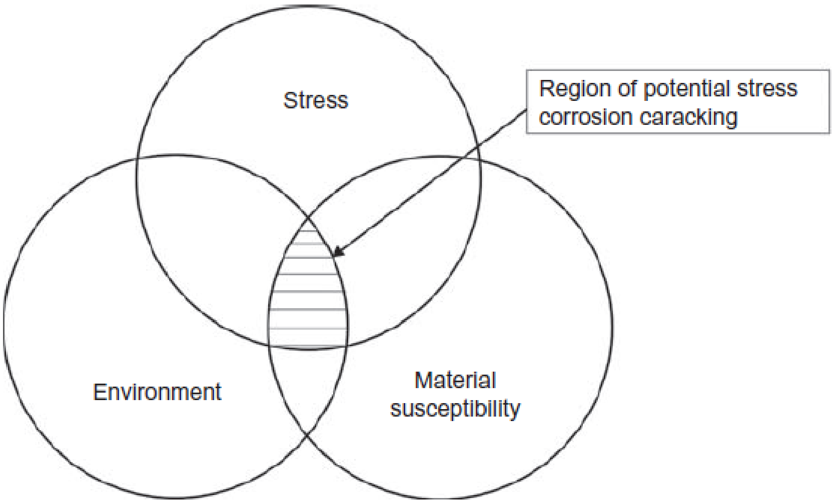

Figure 15 : The classic presentation of SSC includes three circles: material susceptibility, environment, and stress [14].

## 4.2 Stress Corrosion Cracking in BWR Environments

In this section, we will discuss the stress corrosion cracking phenomena in the Boiling Water Reactor (BWR) environments. Ulla Ehrnsten et al. [14] reported the factors that are responsible for initiating SCC in BWRs environments. These factors include degree of sensitization, water chemistry, cold working or deformation, electrochemical corrosion potential (ECP) and other factors.

In another research conducted by Shunichi Suzuki[48], they have observed increased number of SCC occurrences in low carbon stainless steels like type SS 304L & 316L. In the study, they reported that most of the SCC occurred because of cold work and not due to sensitisation. Figure 16 shows a crack initiated in a BWR core shroud cold worked surface layer. Another source of cold work can be cold forming which is sometimes encountered in pipe bends due to inadequate heat treatment or deformations produced during fit-up operations of the piping segments.

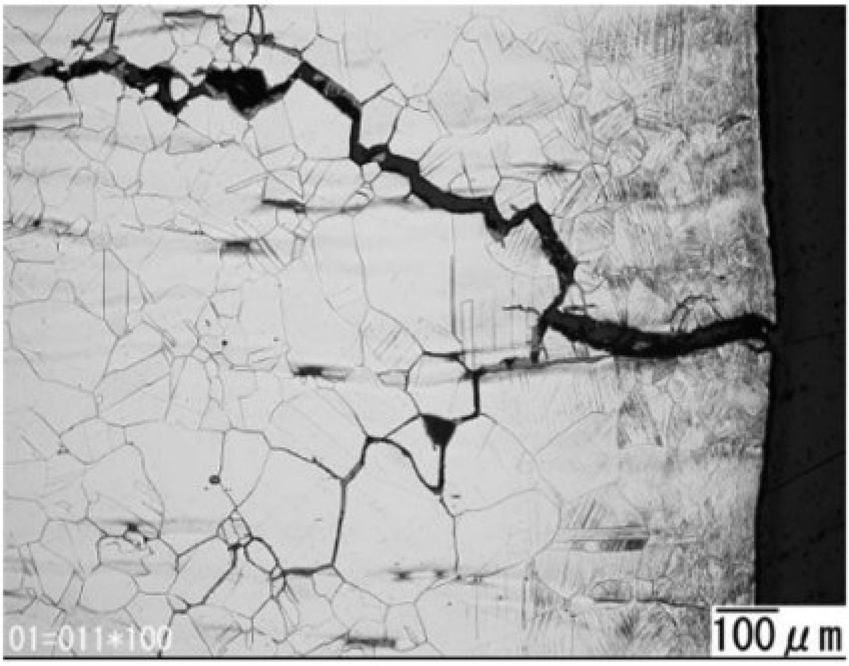

Figure 16 : SSC observed on the edge surface of shroud ring (SUS 316L),adjacent to H6 weld of the core shroud of Fukushima dai-2 Unit 3 [48]

## 4.3 Stress Corrosion Cracking in PWR Environments

In contrast to BWR, the number of SCC failures in austenitic stainless steels are quite small [49]. The small number of SCC failures in PWR environments appears to be in the nominally free flowing conditions, all of which appears to be associated with high level of cold work on the material, which indicates that it might be a prerequisite for crack initiation in austenitic stainless steels. Figure 17 represents the influence of cold work on the cracking of stainless steels in PWR plant environments.

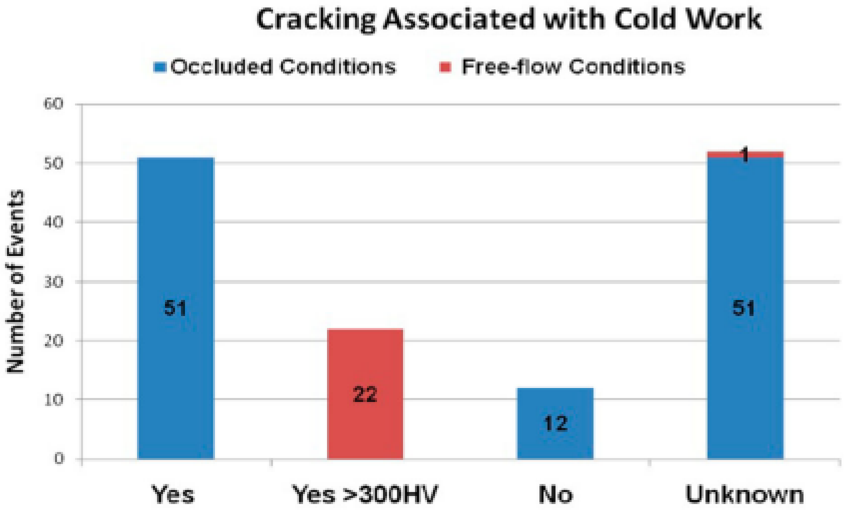

Figure 17 : Influence of cold work on cracking events observed in PWR plant [50].

Despite the small number of cases of SCC failures in stainless steel components exposed to primary water environment, there are various studies in which it is reported that the propagation of a preexisting crack can occur when the material is cold worked up to 15-20%. Shoji et al.[51] studied the deformation behaviour of stainless steels type SS 304L & 316L in the cold worked condition. Figure 18 shows the effects of yield strength on the SCC propagation susceptibility of cold worked type SS 304L & 316L austenitic stainless steels. From the figure, it has been observed that no SSC occurred below a yield strength of 450MPa. However, increasing the deformation level to 750MPa produced SSC with increased growth rates in a simulated PWR environment. There was no significant effect of temperature between 290 and 340°C.

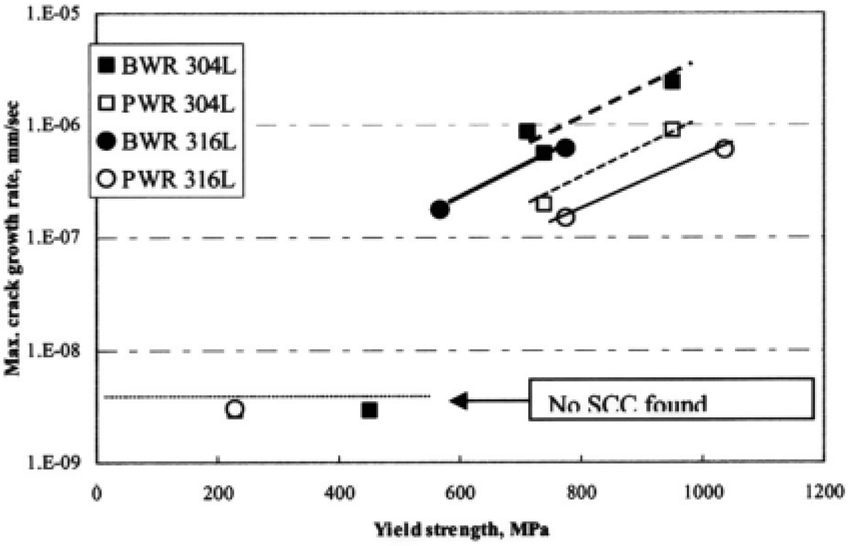

Figure 18 : Effects of yield strength on SCC propagation susceptibility of types 304L and 316L austenitic stainless steels [51].

In another study Nouraei et al. [52] studied the effect of orientation of the cold worked stainless steel sample on the SSC susceptibility in PWR environments. The crack growth rates of specimens tested in three different directions (parallel, transverse, and orthogonal) were studied. The crack growth rate was observed with reference to the original cold worked direction. The parallel direction showed uniform crack growth whereas the in the transverse direction, the crack growth appeared perpendicular to the main fracture surface[53]. Figure 19 shows the optical images of fracture surfaces in different directions with reference to the original cold work direction.

Material composition also plays a significant role in promoting SSC in cold worked stainless steels. Hanninen and Aho.Mantial[54] studied that the lowest sulphur contents of 0.0004%-0.0006% have an appreciable effect in preventing the crack growth rate in type SS 304 or 304L stainless steel. Figure 20 shows the effect of sulphur content on the crack growth rate under constant load. As the sulphur content is increased, the SSC crack growth rate is reduced[55].

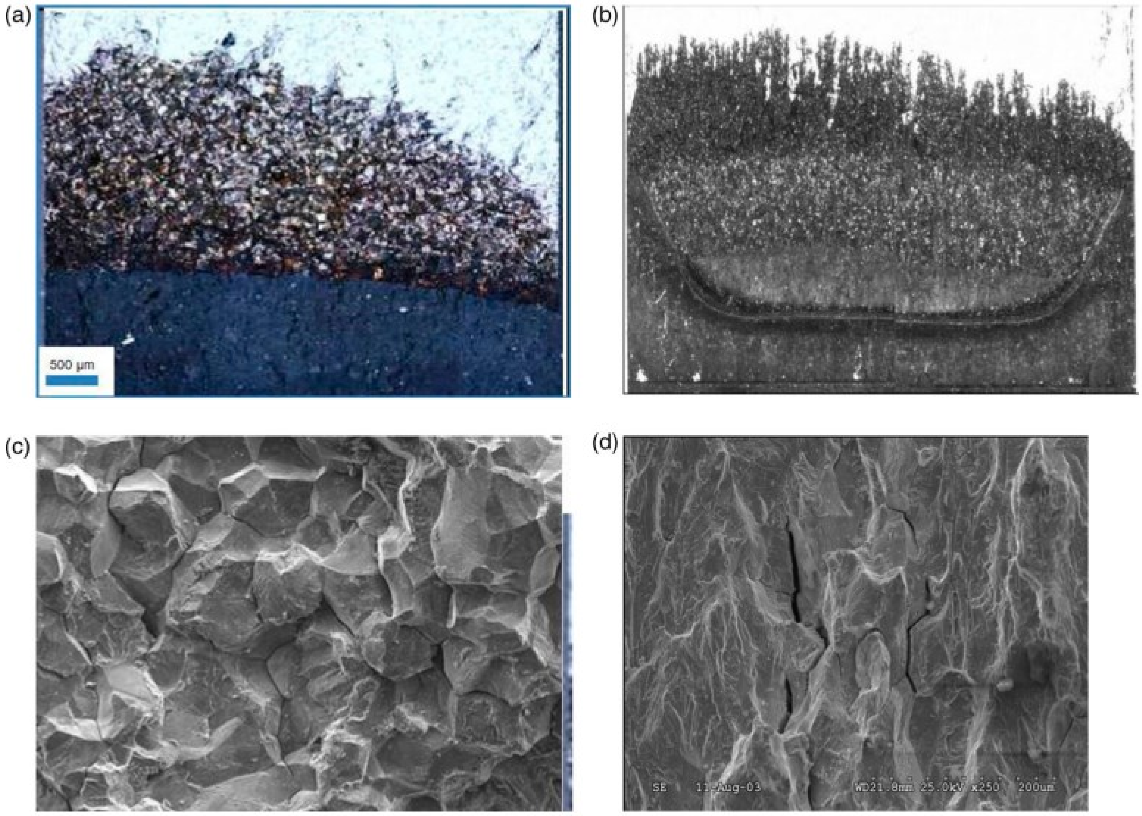

Figure 19 : Optical images of fracture surfaces of S-L specimen (a) and TL specimen and (b) Corresponding SEM images of IG morphology for S-L (c) and mainly transgranular but with secondary IG cracking (d) [52] .

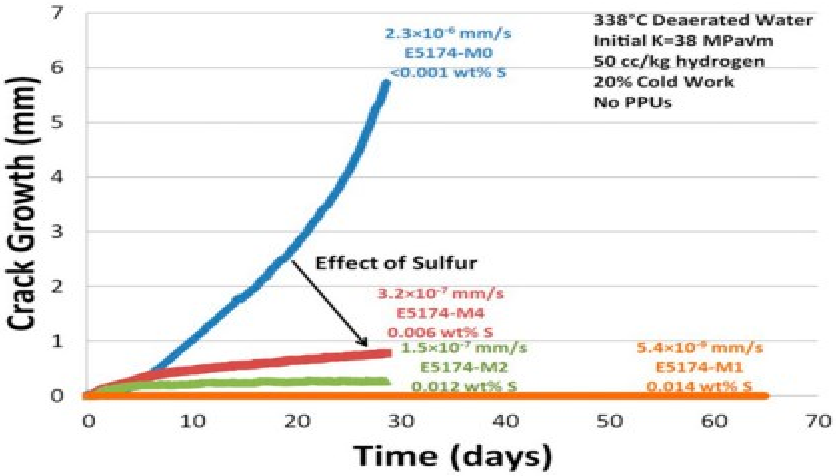

Figure 20 : Results of SSC growth rate test conducted in 338C conducted in deaerated water (a) with an initial K of 38MPa under constant load showing reductions in the SCC growth rate with increasing sulphur content [54] .

## 4.4 Thermally Induced Stress Corrosion Cracking

While SCC has historically been an important failure mechanism for the nuclear industry, in recent times it has been effectively mitigated by careful control of water and alloy chemistry. Thus, SCC cracking in stainless steels piping has not presented problems in recent times, until now. However, the observed cracking indicates that even with the current controlled environment, SCC is still potentially active in some specific circumstances. It is not yet fully understood, what constitutes such specific circumstances. Such understanding is needed to assess the extent of systems at risk and for effective mitigation.

From the published literatures regarding SCC failures, the cracks have occurred in locations that have been identified as potentially subjected to thermal stratification and thermal loads. Thus, thermal loads have been cited as a contributing factor in some studies. The newer plants seem to be more susceptible, and this has been attributed to the design change that increased the risk of thermal stratification and thermal loads, which further supports the role of thermal loads as a contributing factor.

The thermal stresses can potentially promote SCC in several different ways. Firstly, the thermal loads may induce uneven plastic deformation and may leave behind thermal stresses[4].Such thermal residual stresses have previously been used to artificially generate SSC cracks[56].

Furthermore, intermittent load cycles are known to promote SCC and to restart previously stopped crack growth[57]. Therefore, intermittent thermal loads could have a SCC enabling effect in the favourable conditions. Additionally, thermal stresses or repeated thermal stresses can further contribute to strain hardening of the affected material which makes it susceptible to SCC.

### 4.4.1 Thermal Fatigue

Thermal fatigue is one of the major degradation mechanisms studied and researched by the nuclear industry. Thermal fatigue was identified as the cause of leak in the French Civaux Pressurized Water Reactor (PWR) [58]. Yanjun Wang et al. [59] studied the thermal fatigue on AISI 316L(N) austenitic stainless steel samples. The crack initiation and propagation due to thermal cyclic loading was monitored by a hybrid multiview correlation system which enables the investigation of complex thermal fatigue crack networks under thermal variations ranging from 160°C to 230°C. This technique is different from the conventional thermal fatigue measurement techniques [60], [61], [62], [63], [64], [65] because it induces thermal stresses with laser shocks which overcomes the obstacles in the conventional methods due to accurate control of cyclic pulses and a high stability of power density delivered at each impulsion. The cracking mechanisms in the samples were observed via optical microscopy and electron backscattered diffraction (EBSD).

The formation of crack networks under low temperature ranges (170°C and 180°C ) were quite low and only a few sites were able to develop surface cracks. However, when the temperature variation was increased to 230°C, many cracks initiated on the sample surface and a crack network composed of several major and small cracks developed. Figure 21 displays the optical micrograph of the crack network developed during cyclic loading.

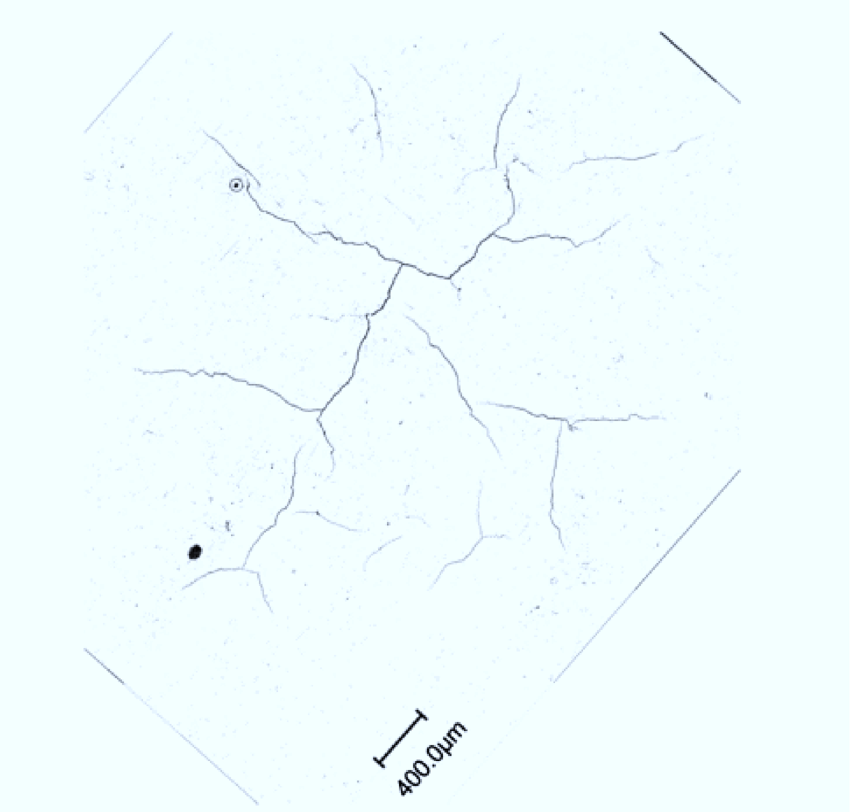

Figure 21 : Optical microscope of the crack network of the specimen when ΔT=230℃ coupled with a static mean tensile stress (σ=15MPa after 21000 cycles [57]

Thermal fatigue is a thermal strain generated by alternating hot and cold water environments. Low cycle fatigue and fatigue crack propagation are generally conducted in high temperature water environments to study the thermal corrosion fatigue service conditions that occurs in pipeline structures of nuclear power plants. During the flow of the medium in the pipeline the hotter and lighter medium will stay above the cooler and heavier medium resulting in a certain temperature gradient which is called thermal stratification [66].

Z.H.li et al. [66] in a study constructed a device that can simulate the influence of transient temperature change on fatigue behaviour of pipeline structures. For typical pressure vessel structures in nuclear power plants, stepped pipe structures were selected to conduct thermal corrosion fatigue crack propagation experiments under transient temperature conditions in a simulated primary circuit environment. The material used in this study was SS 304. The samples were characterized by field emission scanning electron microscopy to observe the crack propagation morphology followed by EBSD analysis to observe the crack propagation area. Thermal fatigue crack propagation is exponentially related to the cooling rate and the critical cooling rate of crack propagation in the weld is 52°C/min. This is because when cold water impacts the hot water inside the stepped pipe from the inlet, the temperature gradient is larger near the inlet resulting in greater thermal stress near the inlet. However, when it moves away from the inlet, the temperature gradient gradually decreases and eventually the thermal stress on the stepped pipe specimen also decreases. Hence, the thermal fatigue crack growth decreases with the decreasing thermal cyclic stress. Figure 22 shows the relationship between the fatigue crack propagation and the cooling rate.

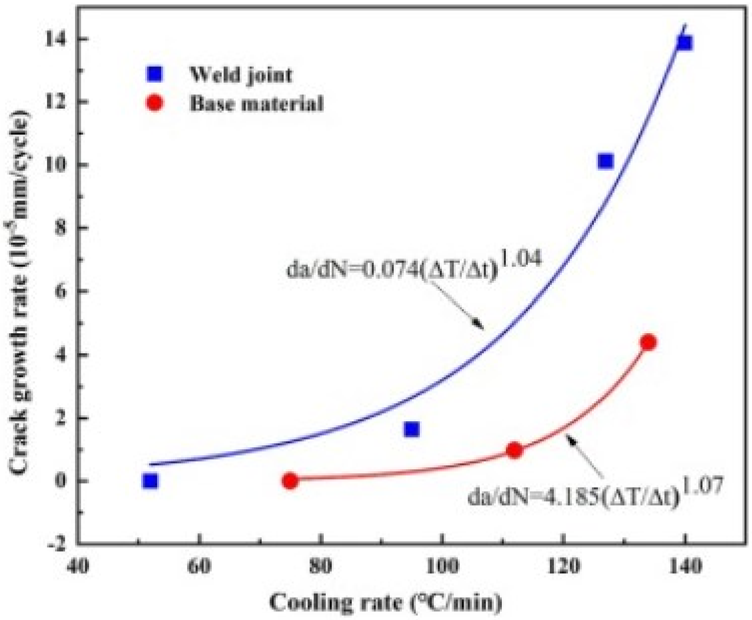

Figure 22 : Relationship between thermal fatigue crack propagation and the cooling rate [64] .

# 5 Experimental Methods

## 5.1 Sample preparation of Welded Pipe Segment

Two rings of pipe of the material type 316L SS were received from VTT from the primary circuit piping segment. The rings were 150 mm in length (diameter, 326mm, thickness 33mm). Figure 23 shows the pipe ring segments. The pipe rings were butt welded together at Suisto Engineering using NG-GTAW method and 316L Si filler metal. Table 1 represents the chemical composition of the pipe. Figure 24 shows the pipe ring segments after being welded together in a butt weld. The butt weld was made using a GMAW wire electrode (THERMANIT GE-316L SI)The chemical composition of the weld metal is listed in Table 2.

Table 1 : Chemical composition of pipe material.

| C | Mn | Si | P | S | Cr | Ni | Mo | Cu | N |
|---|---|---|---|---|---|---|---|---|---|
| **0.028** | 1.81 | 0.39 | 0.022 | 0.002 | 17.1 | 12.03 | 2.27 | 0.56 | 0.08 |

Table 2 ; Weld metal chemical composition

| C | Mn | Si | P | S | Cr | Ni | Mo | Cu | N |
|---|---|---|---|---|---|---|---|---|---|
| **0.02** | 1.6 | 0.85 | 0.023 | 0.002 | 18.3 | 11.4 | 2.5 | 0.2 | 0.073 |

Figure 23 : Pipe ring segments (SS 316L)

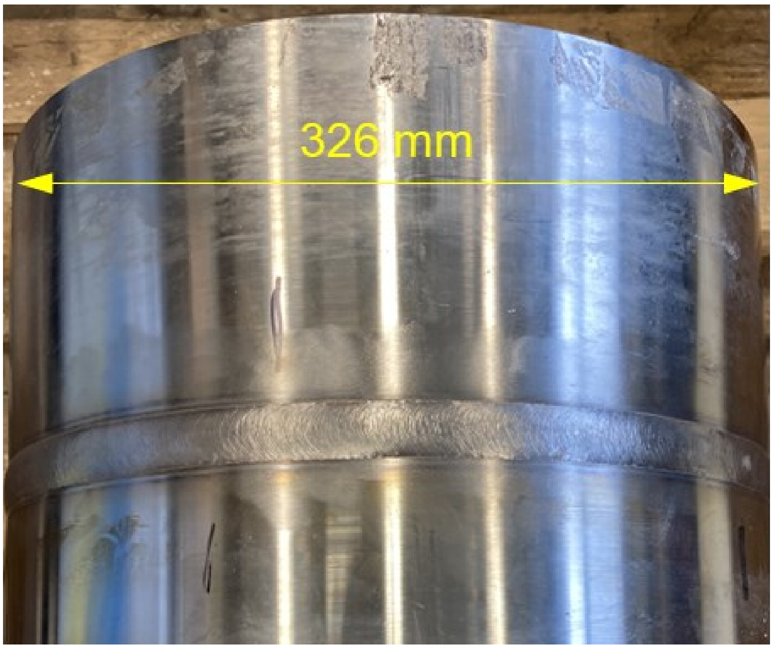

Figure 24 : Butt welded pipe ring segments.

The cutting operation was carried out after the pipes were welded together. A total of three samples were cut from the pipe segment of dimensions (140*65 mm) for the Autoclave SCC testing to be performed at VTT.

A high-power bandsaw was used to cut the samples into the required dimensions. Figure 25 & 26 shows the cutting operation of the pipe segment and the as cut sample from the segment respectively.

Figure 25 : Pipe cutting operation.

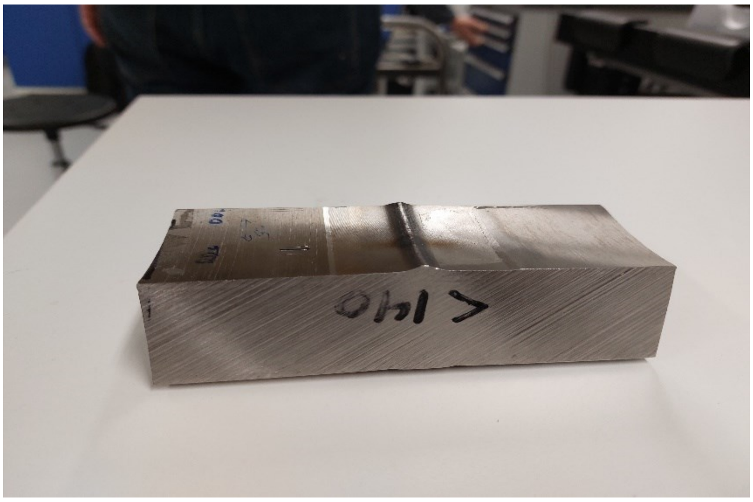

Figure 26 : As cut sample from the pipe ring.

## 5.2 Thermal Cyclic Loading

Thermal cycling loading was performed on the as cut samples. The thermal loading. The thermal loading was introduced at 300,400 & 500℃ from the inner surface of the pipe at 25mm. Figure 27 shows the thermal cyclic loading locations in the pipe segment.

Table 3 lists the parameters used for the thermal cyclic loading in the three cut samples.

Table 3 : Thermal Cycling Parameters

| **Description** | **Value** |
|---|---|
| Heating Time | 4 sec |
| Cooling Time | 30 sec |
| No. of cycles | 3 |

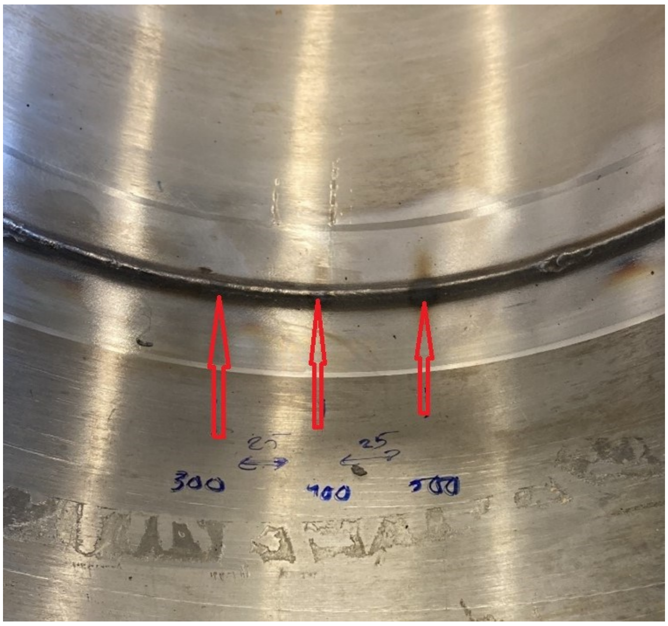

Figure 27 : Thermal cycling loading locations.

## 5.3 Residual Stress Measurements

### 5.3.1 XRD Analysis

The residual stress measurements were carried out on the thermally loaded samples to determine the effect of thermal loading on the residual stresses of the material. These measurements were carried out using XStress 3000 G2R diffractometer. X3000 is the main unit and G2R refers to the type of goniometer. The software used for measuring the residual stress values was Xtronic**.**

Residual Stress measurements were performed from the inner side of the pipe (weld root side) at the weld fusion line , 5 and 25-mm distances from the fusion line respectively. The measurements were done in 3 angles/ directions of 0° (axial), 45° and 90°(hoop). Figure 28 shows the directions of the measured stresses and the location of thermal cycling.

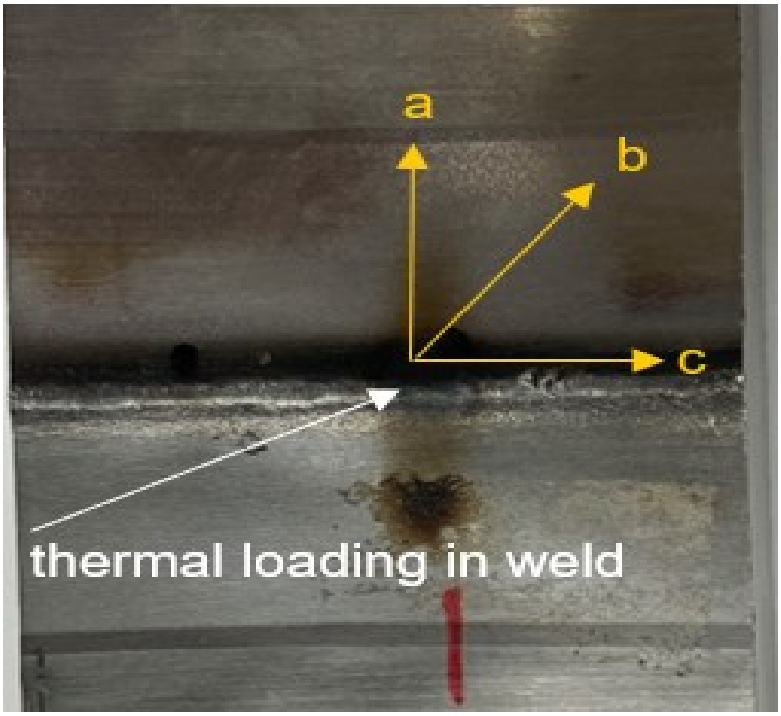

Figure 28 : Measured residual stresses directions.

## 5.4 Metallographic Analysis

In this section, the metallographic operations performed on type 316L SS sample will be discussed. The sample preparation was done by cutting a smaller rectangular section of SS 316 L from the pipe ring keeping the weld area in between.

### 5.4.1 Sample Preparation

The rectangular cross section sample was taken to the Grinding machine where the sample was grinded on different roughness papers. Starting with the 180 grit paper, the grinding continued from coarse to fine by using 360, 800,1200, 2400 and finally the finest paper of 4000 grit.

The sample was then polished to remove the grinding marks and obtain a mirror like structure. The sample was coarse and fine polished. Coarse polishing was done using $3\mu m$ diamond paste. After coarse polishing, the sample was fine polished using $1\mu m$ diamond paste.

The etching was performed on the as polished sample to reveal the microstructure of the material. There are generally many suitable etchants to reveal the microstructure of type 316L SS. However, the best etchant to reveal the microstructure was found to be Beraha II.

Table 4 lists the chemical composition of Beraha II. It is an etchant which is used for revealing the microstructures of austenitic stainless steels. The sample was immersed in the solution of Beraha II for about 10 secs and then taken out.

Table 4 : Chemical Composition of Beraha II

| **Etchant** | **Chemical Composition** | **Quantity** |
|---|---|---|
| Beraha II | Distilled Water | 800 ml |
|  | HCL | 400 ml |
|  | Ammonium Bifluoride | 48g |
|  | Potassium metabisulphite | 2g |

## 5.5 Microstructural Analysis

### 5.5.1 Optical Microscopy

The sample is then taken to optical microscopy for the microstructure analysis of type 316L SS. The etchant (Beraha-II) is a color etchant, and it reveals a colored microstructure of the material. The sample was observed under different objective magnifications of (20X, 50X & 100X) in the optical microscope. Figure 29 shows the setup of optical microscope which was used to observe the microstructure of type 316L SS etched sample.

Figure 29 : Optical microscopy setup.

## 5.6 Mechanical Properties

### 5.6.1 Microhardness Measurements

Microhardness measurements were carried out on the etched sample to determine the hardness of the weld profile and the base material using the Vickers's method. The hardness indentations were taken at three parallel lines distributed equally across the workpiece. Figure 30 shows the hardness indentation lines on the sample. The hardness measurements were carried out using a using Duramin-40 AC2 hardness tester. Table 5 displays the parameters used during the hardness measurements.

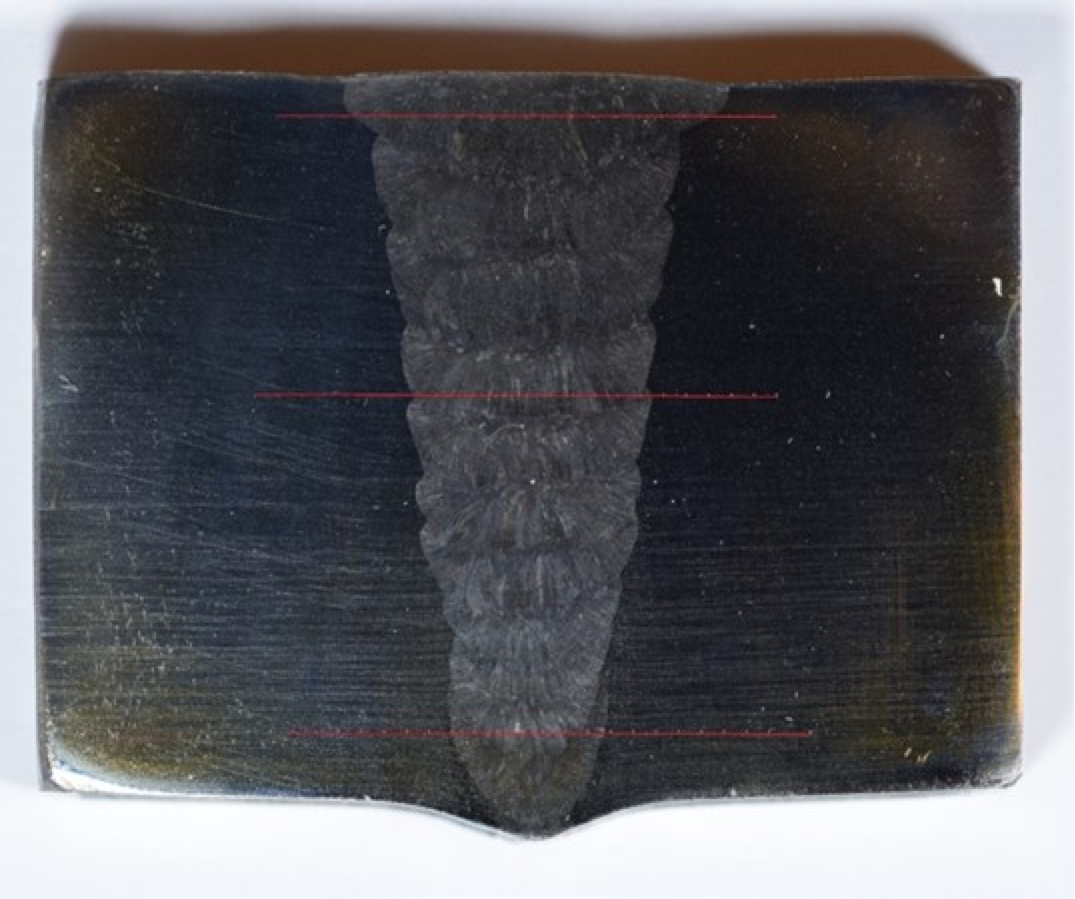

Figure 30 : Hardness indentation points.

Table 5 : Microhardness Measurement Parameters

| **Method** | **Vickers Hardness** |
|---|---|
| **Hardness Scale** | HV1 |
| **Load Applied** | 1 kg |
| **Objective** | 20X |

## 5.7 SCC Test

The Stress Corrosion Cracking (SSC) tests were carried out in the Autoclaves in the PWR environment for the potential SCC developments in the SS 316 L samples. Three samples were subsequently tested in the Autoclaves to determine the susceptibility of the type 316L SS samples to experience SCC. The effect of residual stresses and thermal cycling was observed on the SS316L samples while they were tested in Autoclaves to develop cracks. Figure 31 and 32 shows the test equipment of autoclaves used in the VTT lab. Table 6 shows the testing parameters that are used during the SCC tests.

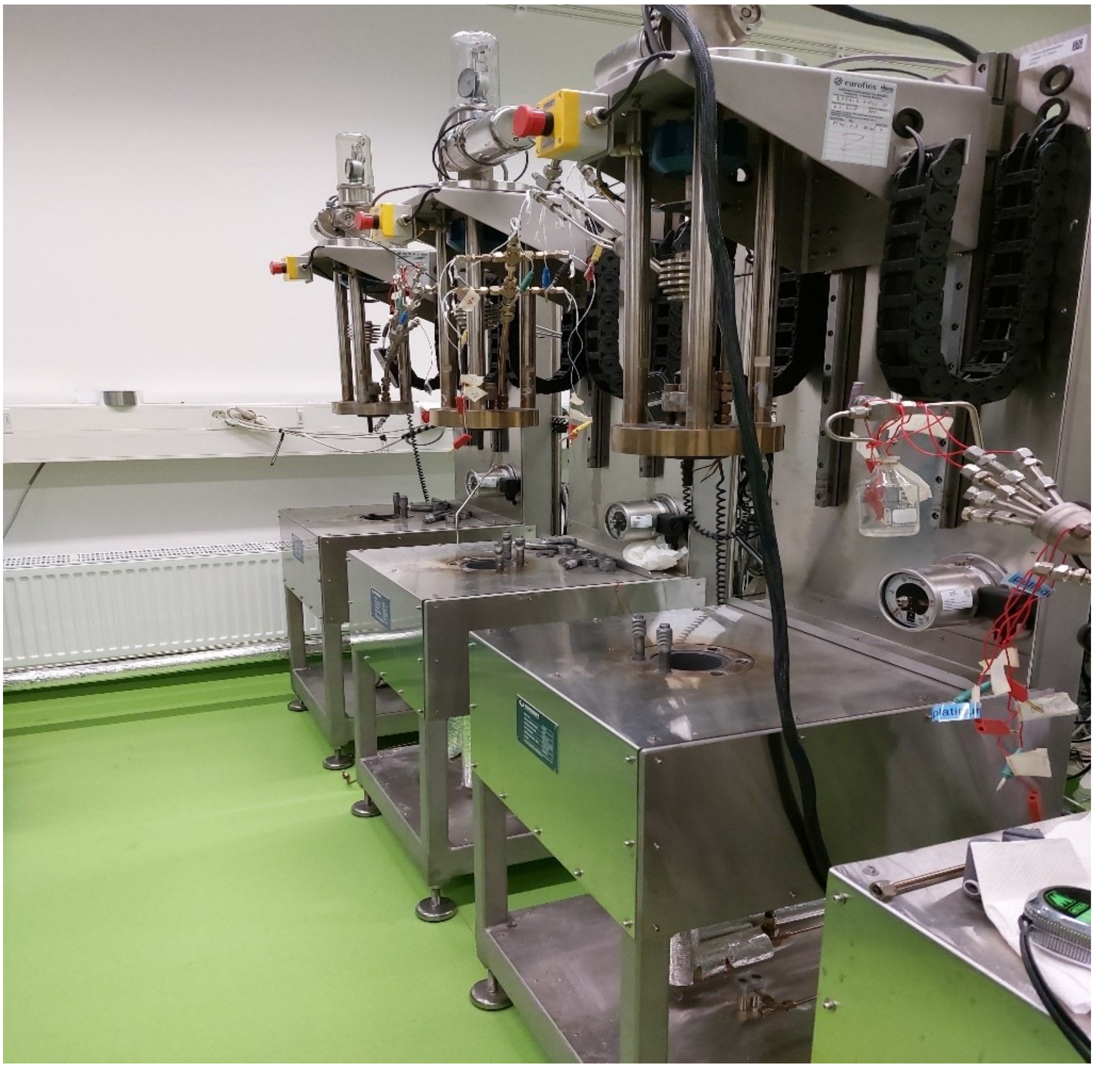

Figure 31 : Autoclaves testing setup at VTT.

Figure 32 : Sample placement in the autoclaves for SCC test.

Table 6 : Testing parameters for SCC test

| **Testing Parameters** | **Values** |
|---|---|
| **Hydrogen water chemistry** | 25 cc/kg |
| **Temperature** | 325℃ |
| **Exposure time** | 4 weeks |
| **External loading** | No |
| **Sample condition monitored during testing** | No |
| **Chamber pressure** | 140 bar |

## 5.8 SEM Analysis

### 5.8.1 Sample Preparation

The stainless steel samples which were subjected to thermal cycling loading at 300°C. 400°C and 500°C were ready for further investigation of potential cracks in the weld metal. The sample thermally cycled at 500°C was prepared for SEM investigation. This involved cutting the sample through weld cross section by wire EDM cutting and then mounting the sample for proper handling. The sample was then grinded and fine polished on automatic grinding and vibrating polishing machine. The vibrating polishing machine used for the experiment was VibroMet. The vibrating polishing solution was colloidal silica with the suspension particle size of 0.04 microns. The vibrating polishing frequency was 100Hz and a time of 6hrs was used. Figure 33 shows the vibrating polishing machine used for sample preparation.

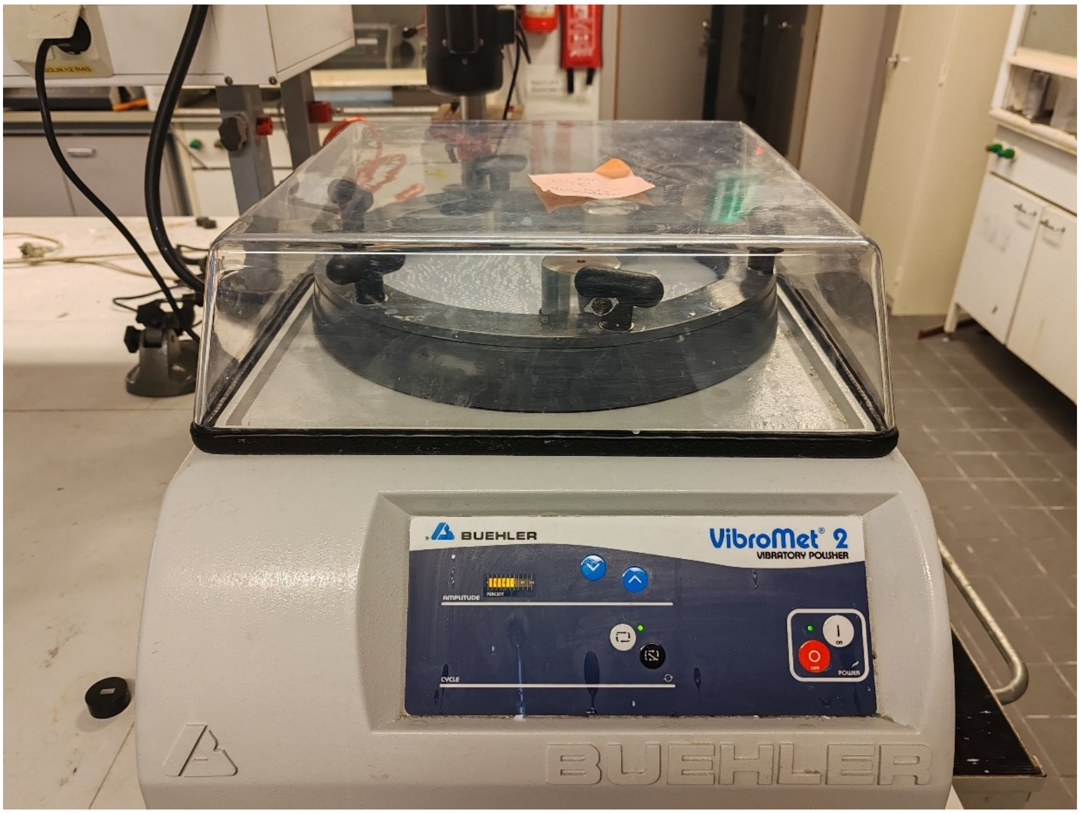

Figure 33 : Vibrating polishing machine.

# 6 Results

This chapter presents the results from the hardness test, the metallography of the SS316L samples, residual stress measurement results on the thermally cyclic loaded samples and the microstructural analysis results followed by brief discussion on these results from the experimental work.

## 6.1 Residual Stress Measurements

The residual stress measurements were taken on the thermal cyclic loaded samples of SS316L before putting the samples in the autoclave for the SCC test. These measurements were carried out on 3 samples. The samples were thermally loaded at 300,400 and 500℃ respectively. The residual stress measurements were carried out at 0, 5 and 25mm from the thermal cycled point for all the samples.  Table 7 present the results of the residual stress measurements.

Table 7 : Residual stress measurement results

| **Angle (°)** | **Distance from the fusion line** | **Thermal loading peak temperature (°C)** | **Residual Stress (MPa)** | **Variation ± (MPa)** |
|---|---|---|---|---|
| **0** | 0 | 500 | 564.6 | 48.2 |
| **45** | | | 458.5 | 33.2 |
| **90** | | | 310.9 | 15.6 |
| **0** | 5 | | 658.0 | 15.7 |
| **45** | | | 514.8 | 16.5 |
| **90** | | | 355.0 | 21.7 |
| **0** | 25 | | -181.5 | 8.7 |
| **45** | | | 23.2 | 15.8 |
| **90** | | | 206.0 | 14.2 |
| **0** | 0 | 400 | 270.2 | 31.6 |
| **45** | | | 157.5 | 20.2 |
| **90** | | | 113.1 | 6.5 |
| **0** | 5 | | 153.5 | 5.4 |
| **45** | | | 143.7 | 9.3 |
| **90** | | | 152.9 | 14.8 |
| **0** | 25 | | -710 | 50.0 |
| **45** | | | -469.0 | 42.1 |
| **90** | | | -222.6 | 34.4 |
| **0** | 0 | 300 | 107.7 | 40.4 |
| **45** | | | 77.9 | 21.8 |

| | | | | |
|---|---|---|---|---|
| **90** | | | 86.1 | 10.3 |
| **0** | 5 | | -146.4 | 18.3 |
| **45** | | | 8.4 | 13.6 |
| **90** | | | 151.5 | 19.1 |
| **0** | 25 | | -669.1 | 60.7 |
| **45** | | | -471.5 | 37.5 |
| **90** | | | -188.6 | 36.0 |

From the results shown in the above table, we can conclude that the thermal cycling produced maximum axial tensile residual stresses at 500°C of around 500 MPa at the distances of 0 and 5 mm from the weld fusion line. Tensile residual stresses at the same distances from the weld fusion line at 400 and 300°C were considerably lower. At 25mm from the weld fusion line, there were compressive residual stresses in all the three temperature cycles (300,400 &500°C).

The locations where compressive residual stresses were observed were far away from the weld metal and the thermally cycled area of the sample. The small effect of cyclic loading in some areas resulted in compressive residual stresses (negative). However, tensile residual stresses were observed in the areas close to the weld metal and thermally cyclic loaded areas. Under cyclic loading conditions, tensile residual stresses can lower the fatigue threshold of stainless steels. This results in crack initiation even at lower stress levels and propagate faster due to the combined effect of cyclic loading and tensile residual stresses. There was some variation in the residual stress values in all three samples, but it can be considered typical to residual stress measurements.

The yield strength of the pipe material was given in the EPR Piping Material Study [67]. The tensile test results at the average room temperature and the material value results were reported in table 2 of the paper [67]. The yield strength, (Rp0.2) [MPa] was reported to be 287 MPa. The residual stresses observed in the experiment were higher than the yield strength of the pipe which in theory is not the ideal scenario. However, since the sample was subjected to thermal cyclic loading , the residual stresses were higher than the yield strength. The welding may have induced strain hardening in the material and that can also be considered one of the factors that contributed to the increased values of tensile residual stresses in the material.

## 6.2 Hardness Measurements

The hardness measurements were carried out on the etched type 316L SS sample. The hardness profiles measured from different locations of the weld cross-section are presented in Figure 34. Table 8 lists the hardness values at different locations of the weld cross section and the location of the measurement.

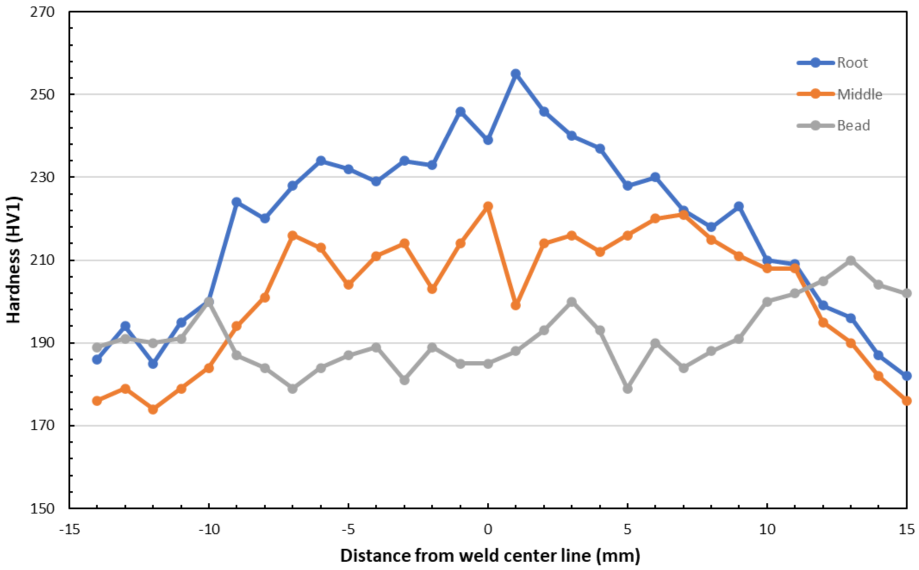

Figure 34 : Hardness profiles (Root, Middle and Bead)

Table 8 : Hardness testing results

| S:NO | Distance from weld centre line | Root | Point location | Middle | Point location | Bead | Point location |
|---|---|---|---|---|---|---|---|
| 1 | -14 | 186 | Base Material | 176 | Base Material | 189 | Base Material |
| 2 | -13 | 194 | Base Material | 179 | Base Material | 191 | Base Material |
| 3 | -12 | 185 | Base Material | 174 | Base Material | 190 | Base Material |
| 4 | -11 | 195 | Base Material | 179 | Base Material | 191 | Base Material |
| 5 | -10 | 200 | Base Material | 184 | Base Material | 200 | Base Material |
| 6 | -9 | 224 | Base Material | 194 | Base Material | 187 | Base Material |

| | | | | | | | |
|---|---|---|---|---|---|---|---|
| **7** | -8 | 220 | Base Material | 201 | Base Material | 184 | Base Material |
| **8** | -7 | 228 | Base Material | 216 | Base Material | 179 | Base Material |
| **9** | -6 | 234 | Base Material | 213 | Base Material | 184 | Weld |
| **10** | -5 | 232 | Base Material | 204 | Base Material | 187 | Weld |
| **11** | -4 | 229 | Base Material | 211 | Weld | 189 | Weld |
| **12** | -3 | 234 | Base Material | 214 | Weld | 181 | Weld |
| **13** | -2 | 233 | Weld | 203 | Weld | 189 | Weld |
| **14** | -1 | 246 | Weld | 214 | Weld | 185 | Weld |
| **15** | 0 | 239 | Weld | 223 | Weld | 185 | Weld |
| **16** | 1 | 255 | Weld | 199 | Weld | 188 | Weld |
| **17** | 2 | 246 | Weld | 214 | Weld | 193 | Weld |
| **18** | 3 | 240 | Weld | 216 | Weld | 200 | Weld |
| **19** | 4 | 237 | Base Material | 212 | Weld | 193 | Weld |
| **20** | 5 | 228 | Base Material | 216 | Weld | 179 | Weld |
| **21** | 6 | 230 | Base Material | 220 | Weld | 190 | Weld |
| **22** | 7 | 222 | Base Material | 221 | Base Material | 184 | Weld |
| **23** | 8 | 218 | Base Material | 215 | Base Material | 188 | Base Material |
| **24** | 9 | 223 | Base Material | 211 | Base Material | 191 | Base Material |
| **25** | 10 | 210 | Base Material | 208 | Base Material | 200 | Base Material |
| **26** | 11 | 209 | Base Material | 208 | Base Material | 202 | Base Material |
| **27** | 12 | 199 | Base Material | 195 | Base Material | 205 | Base Material |
| **28** | 13 | 196 | Base Material | 190 | Base Material | 210 | Base Material |
| **29** | 14 | 187 | Base Material | 182 | Base Material | 204 | Base Material |
| **30** | 15 | 182 | Base Material | 176 | Base Material | 202 | Base Material |

From the chart and the table for hardness profiles, we can observe that the hardness values were the greatest in the weld root location being of order of 250 HV1 at maximum. The lowest hardness values were measured on the bead side of the weld. The hardness of the base material was below 200 HV1, which is typical for the pipe material in solution annealed and quenched condition.

The lowest hardness values were observed in the base metal because it has gone the least amount of thermal processing and solution annealing heat treatment reduces the hardness of the material. However, due to welding and residual stresses in the weld metal and the heat affected zone (HAZ), the hardness values were the greatest in the middle area of the sample.

## 6.3 Microstructure Analysis

### 6.3.1 Optical Microscopy

The microstructure analysis of the ss316L sample was carried out using an optical microscope at different magnifications. Figure 35 represents the microstructure of the weld sample taken from the middle of the pipe weld cross-section.

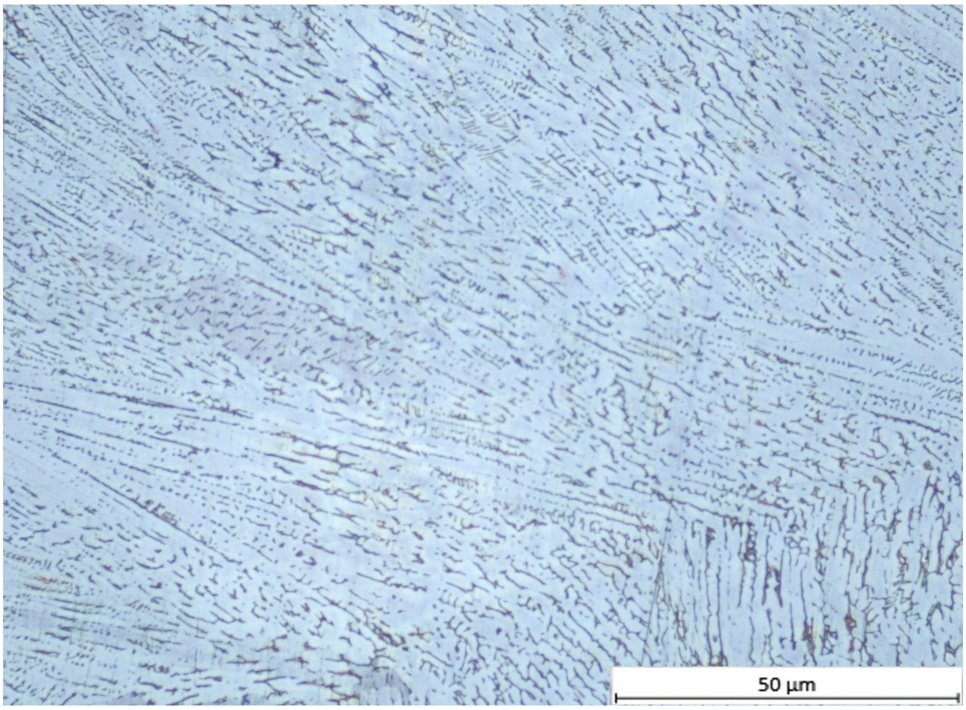

(a)

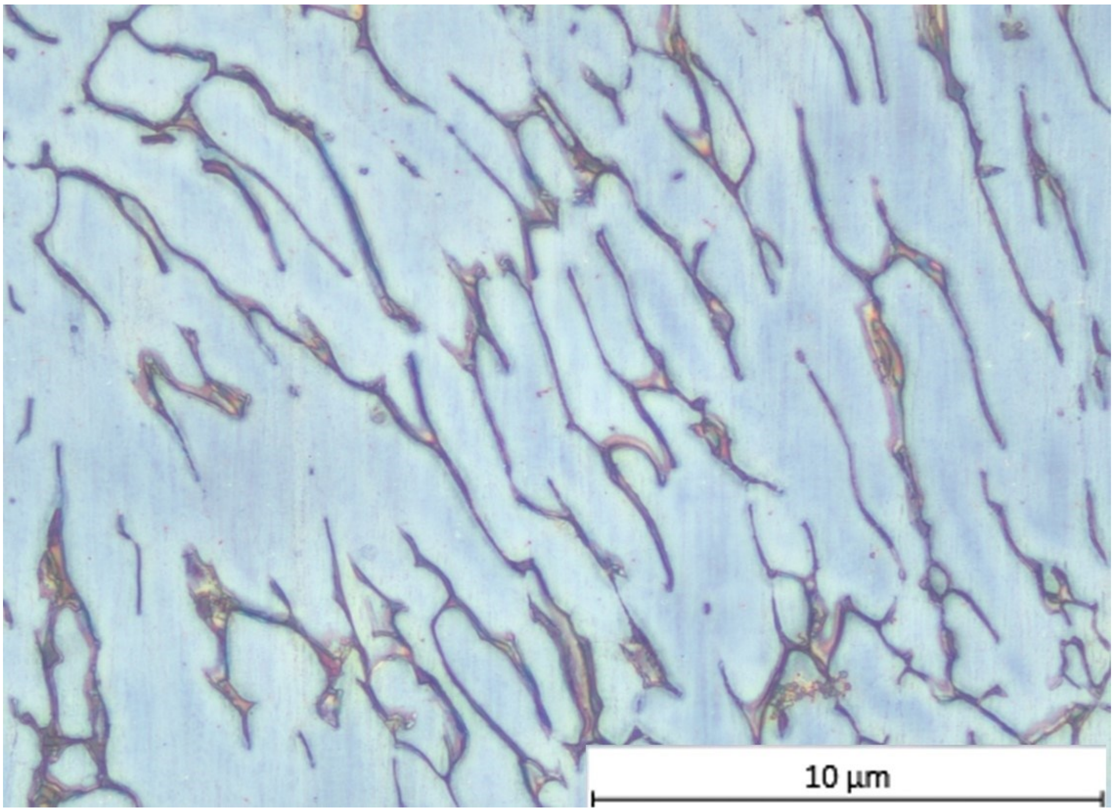

(b)

Figure 35 : Optical microscopic structures of etched SS 316L (a) shows homogenous austenitic structure with austenite grains distributed in the matrix taken at 20X (b) shows the austenitic structure with some retained ferrite due to welding and thermal cyclic loading at 100X (weld metal)

The microstructures were taken at objectives of 20x and 100x. The microstructure at 20x is uniform throughout the weld having a typical dendritic weld microstructure. The predominant phase in type 316L SS is the austenitic phase which has face centred cubic (FCC) crystal structure. The austenitic phase has uniform grain size and distribution through the matrix. The thin dark lines in the microstructure represents the grain boundaries in the austenitic matrix. There are some non-metallic inclusions that can be seen as some dark spots or lines.

The microstructure at 100x shows large, light etching regions which are consistent with the austenitic grains. The grains appear equiaxed which indicates that the steel has undergone a process of annealing at high temperature followed by quenching.

The base material microstructure was also observed using the optical microscope. The base material microstructure was observed at 100X magnification. Figure 36 shows the base material microstructures of SS 316 sample.

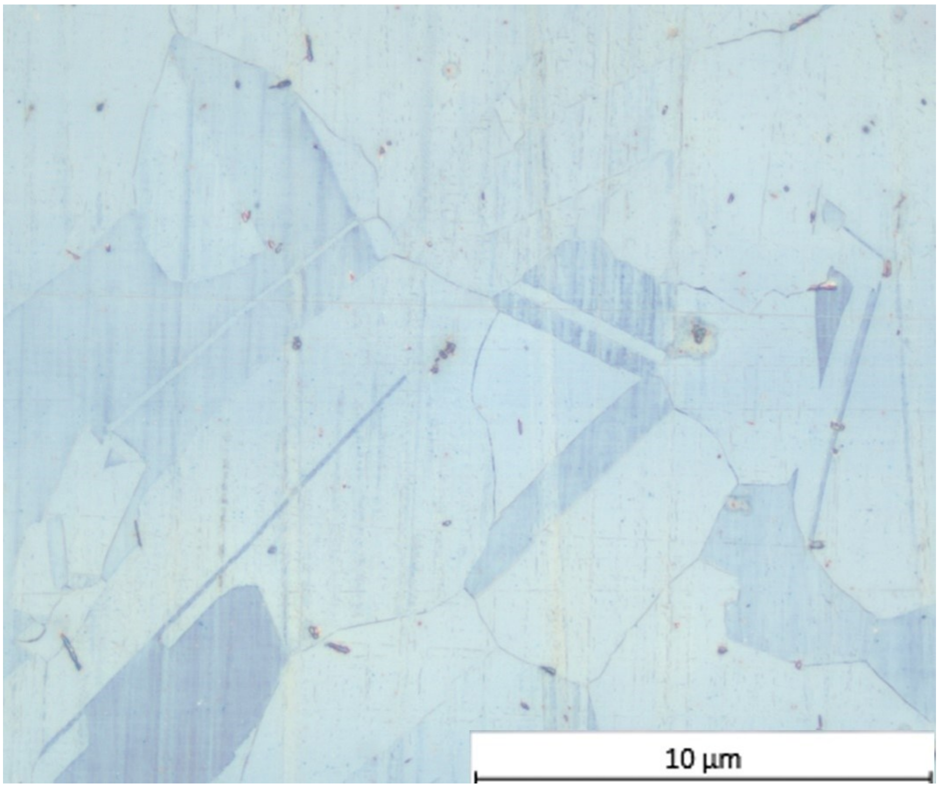

Figure 36 : Optical microscope structure at 100X (base metal)

### 6.3.2 SEM Investigation

This section will present and discuss the results of the SEM analysis on the type 316L SS samples that were subjected to thermal cyclic loading followed by SSC testing in the autoclaves. The sample cycled at 500°C was used for SEM investigation. Figure 37 represents the SEM images of weld metal cross section taken at different and higher magnifications.

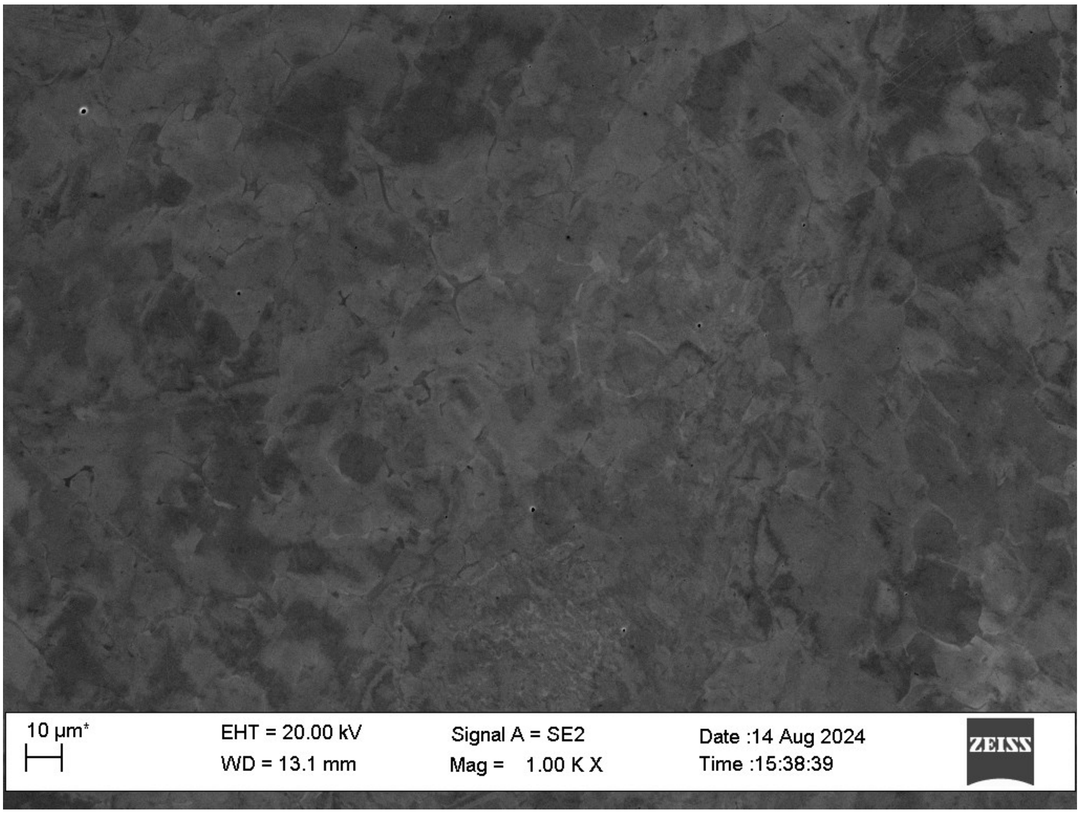
10 µm*
EHT = 20.00 kV
WD = 13.1 mm
Signal A = SE2
Mag = 1.00 K X
Date :14 Aug 2024
Time :15:38:39
ZEISS

(a)

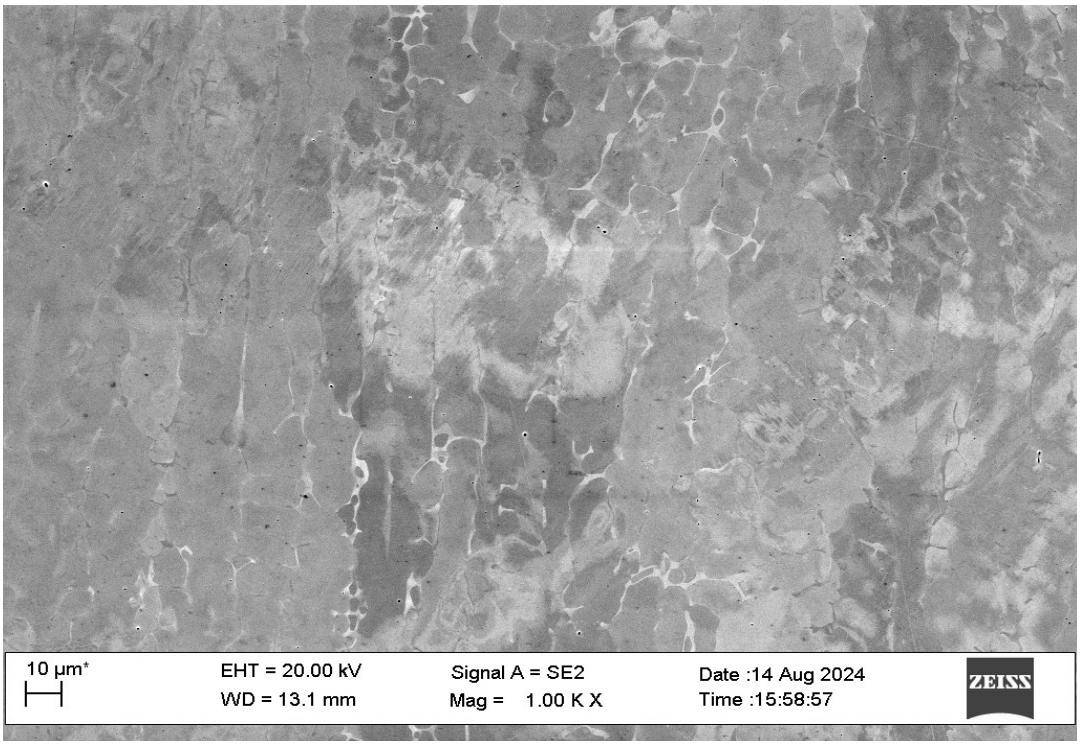
10 µm*
EHT = 20.00 kV
WD = 13.1 mm
Signal A = SE2
Mag = 1.00 K X
Date :14 Aug 2024
Time :15:58:57
ZEISS

(b)

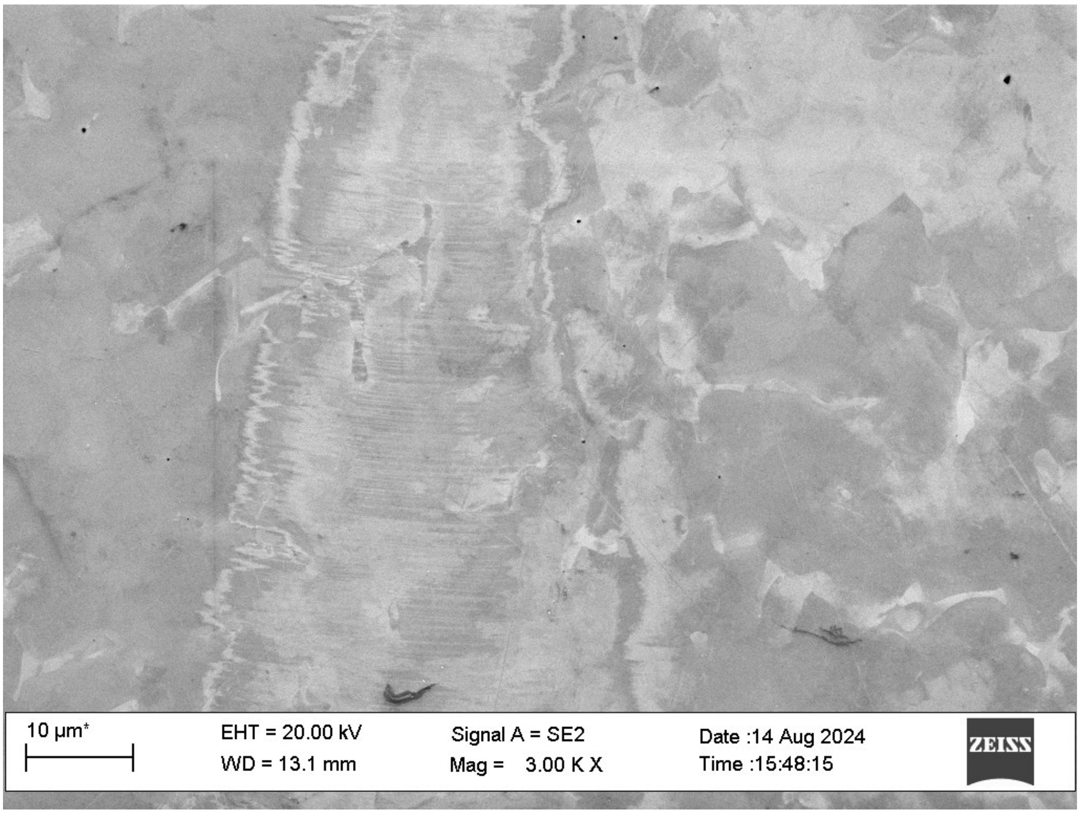
10 µm*
EHT = 20.00 kV
WD = 13.1 mm
Signal A = SE2
Mag = 3.00 K X
Date :14 Aug 2024
Time :15:48:15
ZEISS

( c )

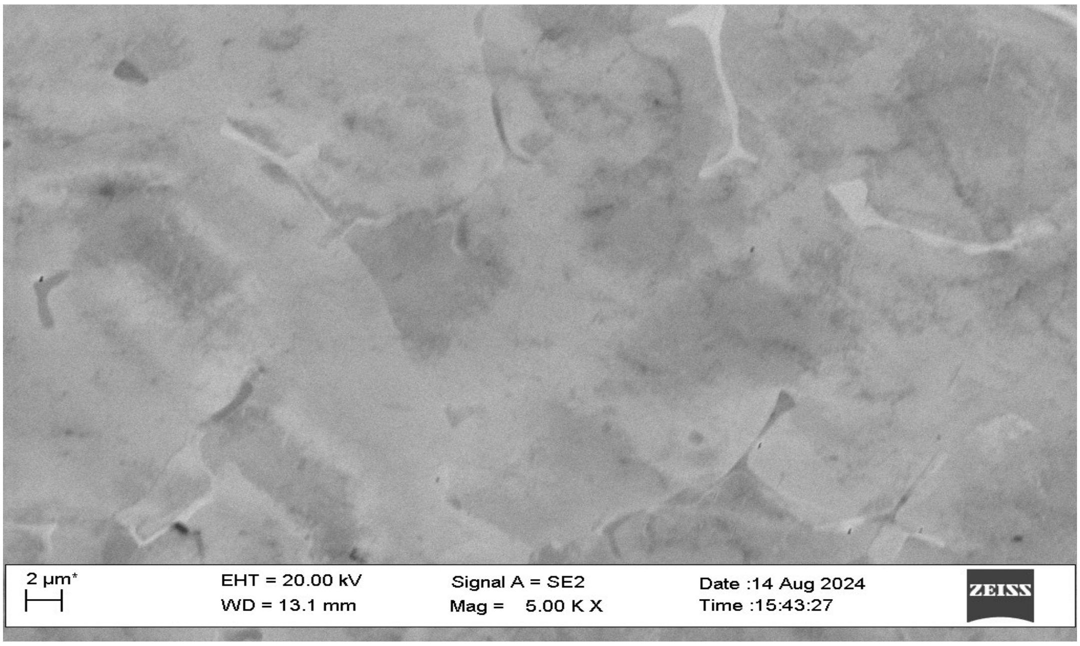
2 µm*
EHT = 20.00 kV
WD = 13.1 mm
Signal A = SE2
Mag = 5.00 K X
Date :14 Aug 2024
Time :15:43:27
ZEISS

(d)

Figure 37 : SEM Images of SS316L in as polished condition. The images show the austenitic grains along with some inclusions from the silica paste from the vibrator polisher (a) at 1000X (b) at 1000X (c) at 3000 K X (d) at 5000X

The SEM investigation revealed the weld metal cross section at higher magnifications. From the figures, it was observed that the structure was quite uniform while there were no signs of any cracks in the weld metal. There were some inclusions which can be seen as black dots in the images. However, there were no evident cracks visible in the microstructure. This can be attributed to the fact the even though type 316L SS is susceptible to stress corrosion cracking in corrosive environments and under cyclic thermal loading, the material did not develop cracks and we observed a crack free weld metal from the analysis.

The SS316L samples were exposed to PWR environment in the autoclaves at VTT for a period of 4 weeks. The exposure time required to develop any cracks in the sample which is subjected to thermal cyclic loading and containing residual stresses may vary between 4-12 weeks. As we did not observe any cracks in the highly loaded sample (thermal cycled at 500°C), it is a possibility that less exposure time given to the samples may be one of the factors that may have contributed to a crack free type 316L SS weld.

As discussed in Chapter 4 of this thesis, cold working is one the most significant contributing factor in increasing the susceptibility of stainless steels to stress corrosion cracking when exposed to corrosive environments. In this case, the welding of the pipe material was not sufficient to induce cold working in the material and therefore local regions in the weld area of the pipe segment were subjected to thermal loads to create a variation of potential thermal load effects. This resulted in the formation of residual stresses which were supposed to induce sufficient plastic deformation or cold work in the material that when exposed to simulated PWR environments may develop some cracks. However, contrary to our expectations, the cracks were not developed even in the highly loaded samples.

## 6.4 Material Characterization

### 6.4.1 EBSD Analysis

Electron Backscattered Diffraction (EBSD) analysis was carried out on the sample to observe the non-uniformity of microstructure, crystallographic orientation, phase distribution and misorientation within the grains. The analysis was carried out on 500x and 1000x magnification using SEM. The analysis was carried out on the welded cross section of the sample and the analysis points were taken at the thermal loading area from the top of the weld to the bottom (root) of the weld. Figure 38 shows the points taken for the EBSD analysis from the sample prepared.

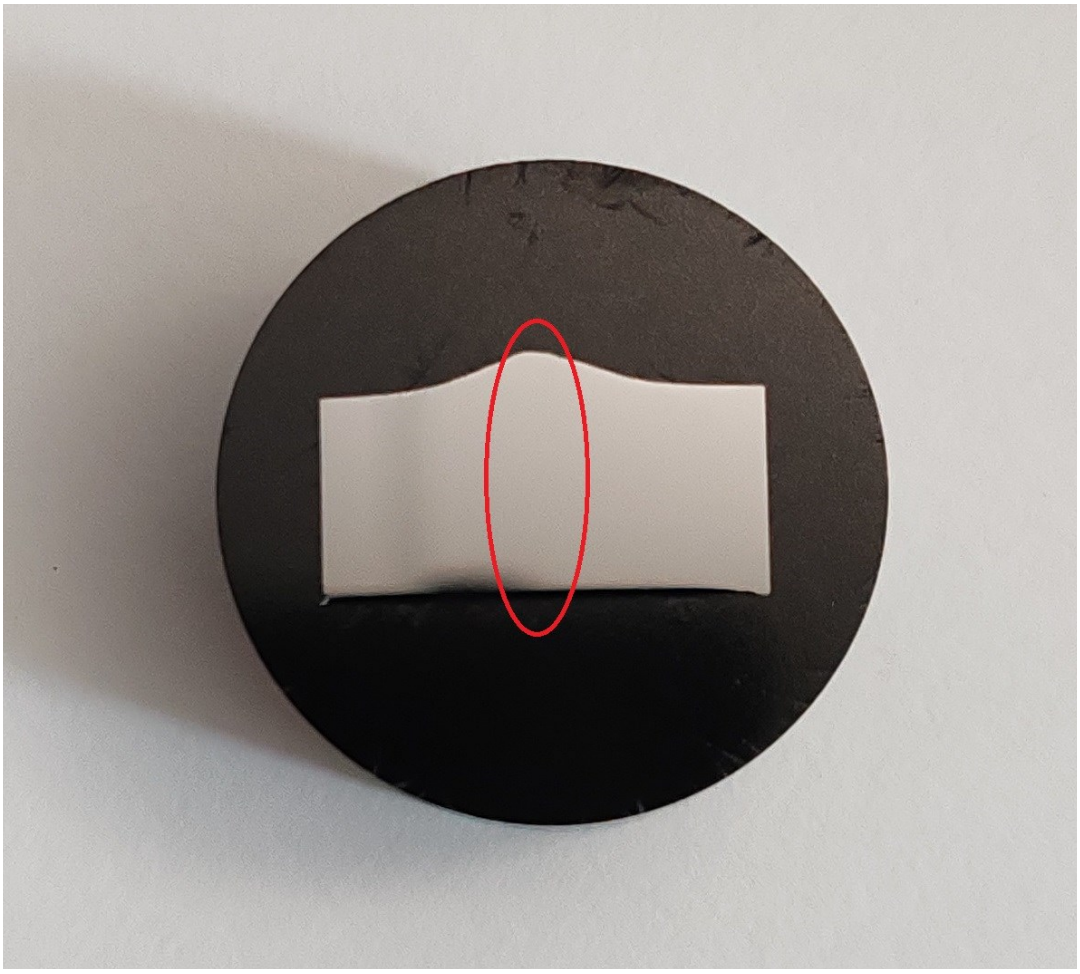

Figure 38 : Weld metal points for EBSD analysis.

#### 6.4.1.1 IPF Orientation Maps

IPF (inverse pole figure) represents the crystallographic orientation of grains in polycrystalline materials. IPF shows colors according to which direction or planes are with respect to the reference axis. IPF uses a color key according to which it represents the crystallographic orientation of the grains relative to a specified direction. The color key is a triangle that represents the crystallographic directions. The triangle corners represent the basic crystallographic axis. Figure 39 shows the color key of the IPF that has been used in the current analysis. The IPF orientation maps obtained from the weld cross section are shown in figure 40.

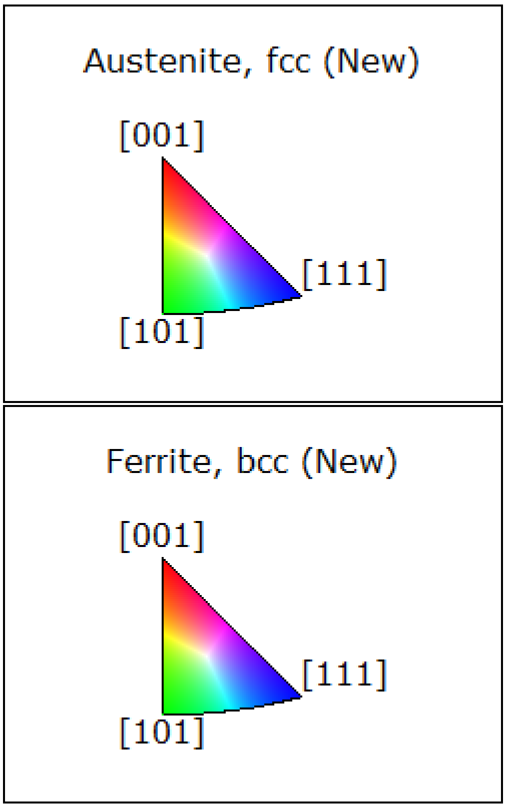

Figure 39 : IPF color key for Austenite (fcc) and Ferrite (bcc)

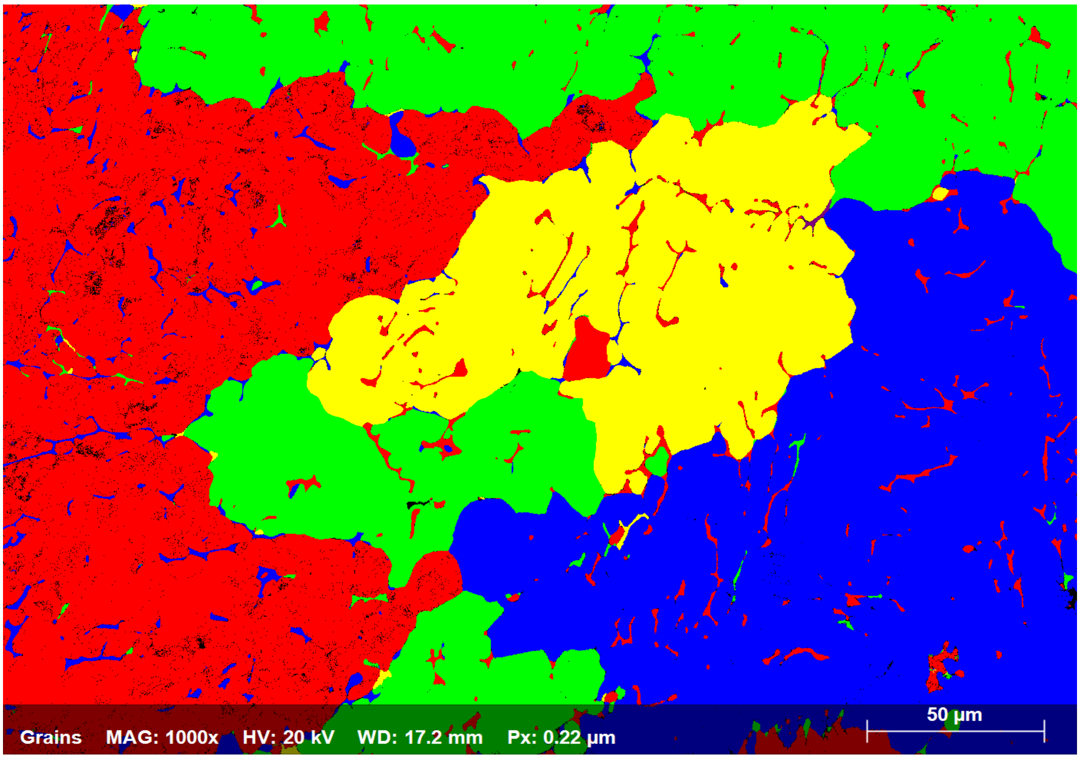
Grains MAG: 1000x HV: 20 kV WD: 17.2 mm Px: 0.22 µm
50 µm

(a)

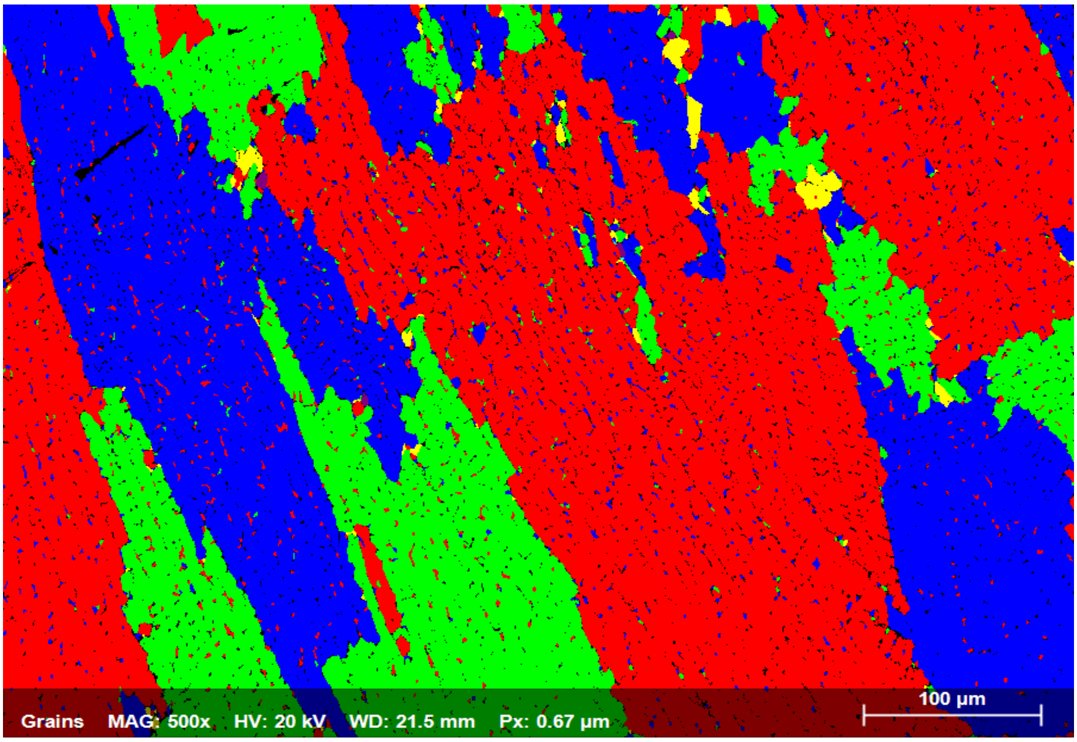
Grains MAG: 500x HV: 20 kV WD: 21.5 mm Px: 0.67 µm
100 µm

(b)

Figure 40 : EBSD-IPF orientation maps for weld metal points showing large and non-uniform grains. The different color schemes represent the orientation that corresponds to [100], [101], or [111] directions (a) at 1000X (b) at 500X.

The above figures represent the IPF grain maps for the type 316L SS sample being examined. The fully saturated colors represent orientations close to the exact [100], [110], or [111] directions. However, there are some yellowish regions in the grain maps and that could represent orientation that is intermediate between these directions. From the images, it is evident that due to welding and thermal stresses in the material, there has been diffusion less transformation in the material and we can observe large grains in the material. Although the structure looks mostly authentic it is type 316L SS, we can see some ferrite which has been retained due to the welding operation in figure 40 (a) . Figure 40 (b) represents more directional solidification, and the grain-to-grain orientation may vary within the crystal structure.

We will compare these grain maps with the base material crystallographic orientation maps and would observe the difference that can be observed due to welding and thermal stresses that were applied on the material. The base material points were taken from the edge of the sample as shown in figure 41. Figure 42 displays the orientation maps for the base material points.

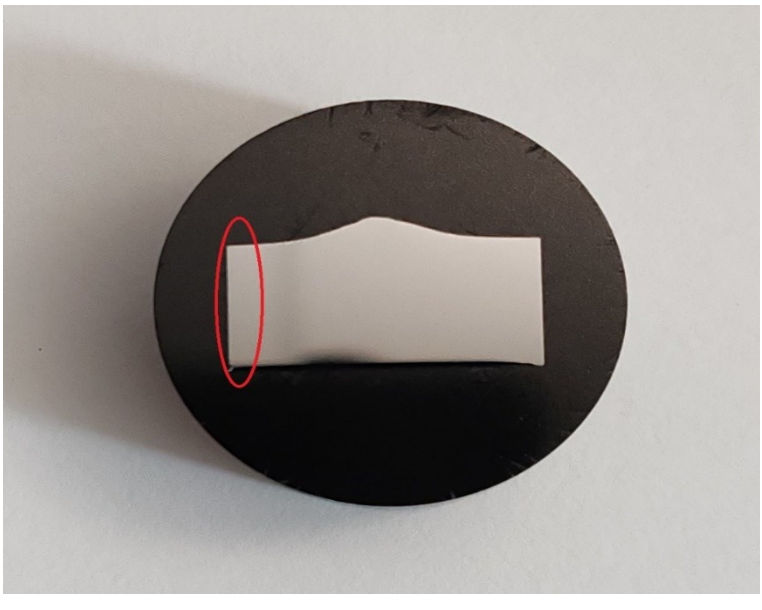

Figure 41 : Base metal points for EBSD analysis.

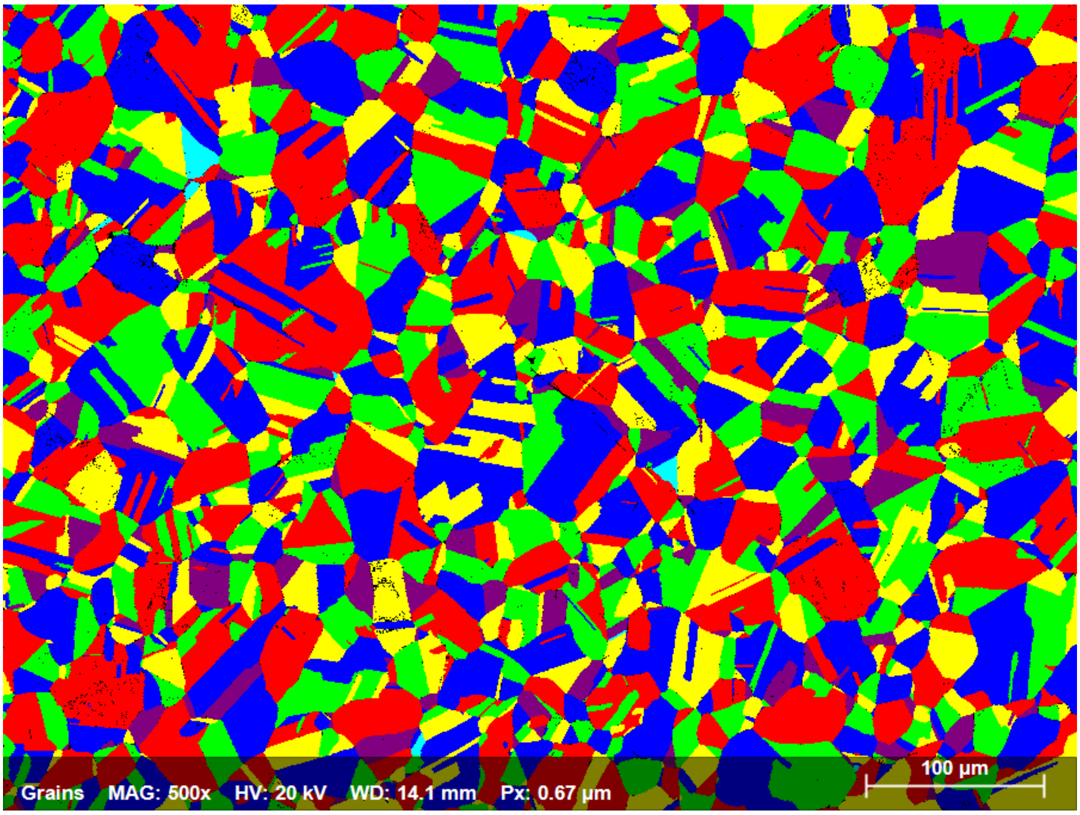

Figure 42 : EBSD-IPF orientation map for base metal points representing equiaxed austenite grains. The uniform grain size indicates minimal or no affect of thermal stresses and welding on the base metal.

The above IPF orientation map is obtained from the base material of type 316L SS. The base material has minimal or no effect of welding and thermal cyclic loading since it is away from the thermal loading areas in the weld metal. The orientation map obtained shows equiaxed grains and the differences in the grain size are not obvious. This is because there has been no effect of welding and thermal stresses in the base material and we can observe a pretty good crystallographic orientation within the grains.

#### 6.4.1.2 Phase Maps

Phase maps in the EBSD analysis provides information about the different crystalline phases present in the material. Phase maps are a powerful tool to analyze the exact phases and their distribution within the material. In phase maps, each phase is distinguished by a unique color. This color is assigned to the phases by the software based on the crystallographic data obtained during the EBSD analysis. The software builds a map showing the location and distribution of different phases. In our study, we worked on the type

316L SS sample and obtained the phase maps from both the welded cross section and the base material points. Figure 43 (a) represents the phase map obtained from the weld area.

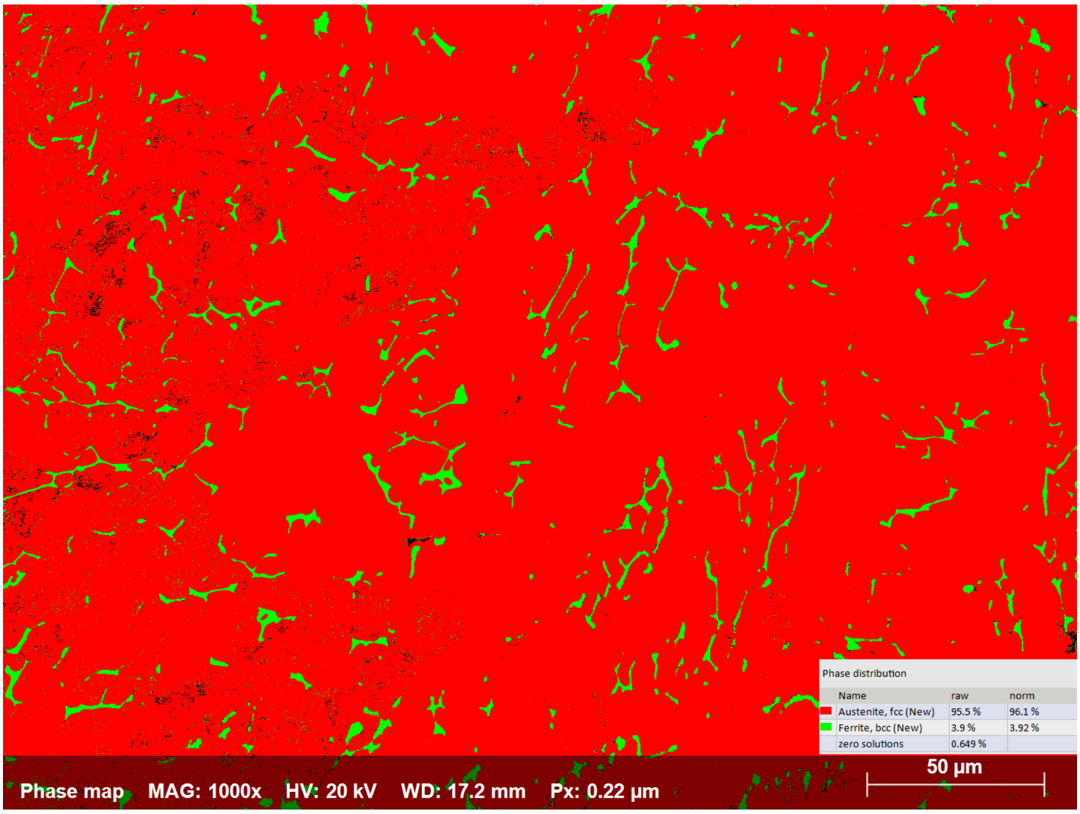

Phase distribution

|  | Name | raw | norm |
|---|---|---|---|
| 🟥 | Austenite, fcc (New) | 95.5 % | 96.1 % |
| 🟩 | Ferrite, bcc (New) | 3.9 % | 3.92 % |
|  | zero solutions | 0.649 % |  |

(a)

The above phase map is obtained from the weld area of the sample where the effect of welding and thermal loading is maximum, and it can be seen in the phase map as well. In the phase map, we can observe the red colored austenitic (fcc) structure along with the green colored ferrite (bcc) which is nucleated during the solidification process in the welding. During solidification, type 316L SS can go under ferritic-austenitic solidification mode depending on the cooling rate. A fast cooling rate can retain some ferrite in the microstructure even after the material cools down to room temperature.

We will compare this phase map with the one obtained from the base material and would see the difference between the two phase maps. The phase map obtained from the base material points is shown in figure 43 (b)

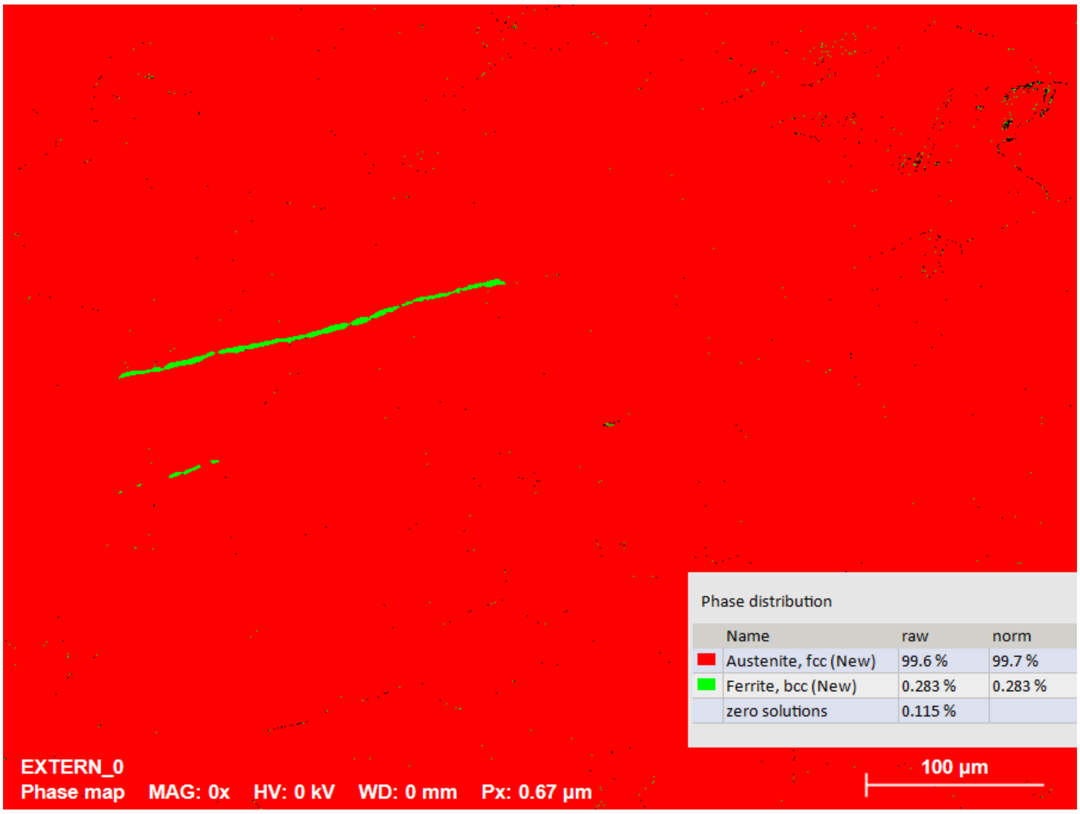

(b)

Figure 43 : Phase maps for (a) weld metal (b) base metal. The phase maps represent the % of austenite and ferrite in the SS 316L sample and the % of zero solutions.

The above phase map illustrates that the phase distribution in the material. The red colored area is austenite (fcc) while the green colored line shown in the map could be recrystallized ferrite. This small amount of ferrite observed can also be the result of any prior processing or cold work on the material before welding. Some inhomogeneities in the microstructure or residual stresses that cause localized changes in the phase stability which results in the formation of ferrite in certain regions of the base material. Overall, the structure is fully austenitic which indicates that there has been very little or no nucleation of ferrite in the base material.

#### 6.4.1.3 MO Average Maps

In EBSD, the MO average maps are used to visualize the average misorientation within the grains of a polycrystalline material. The MO maps are used to observe the strain accumulated at the grain boundary between the phases. The misorientation is the angular difference between the crystallographic orientations of two adjacent grains. The MO average map obtained in this analysis for the weld area is shown in figure 44.

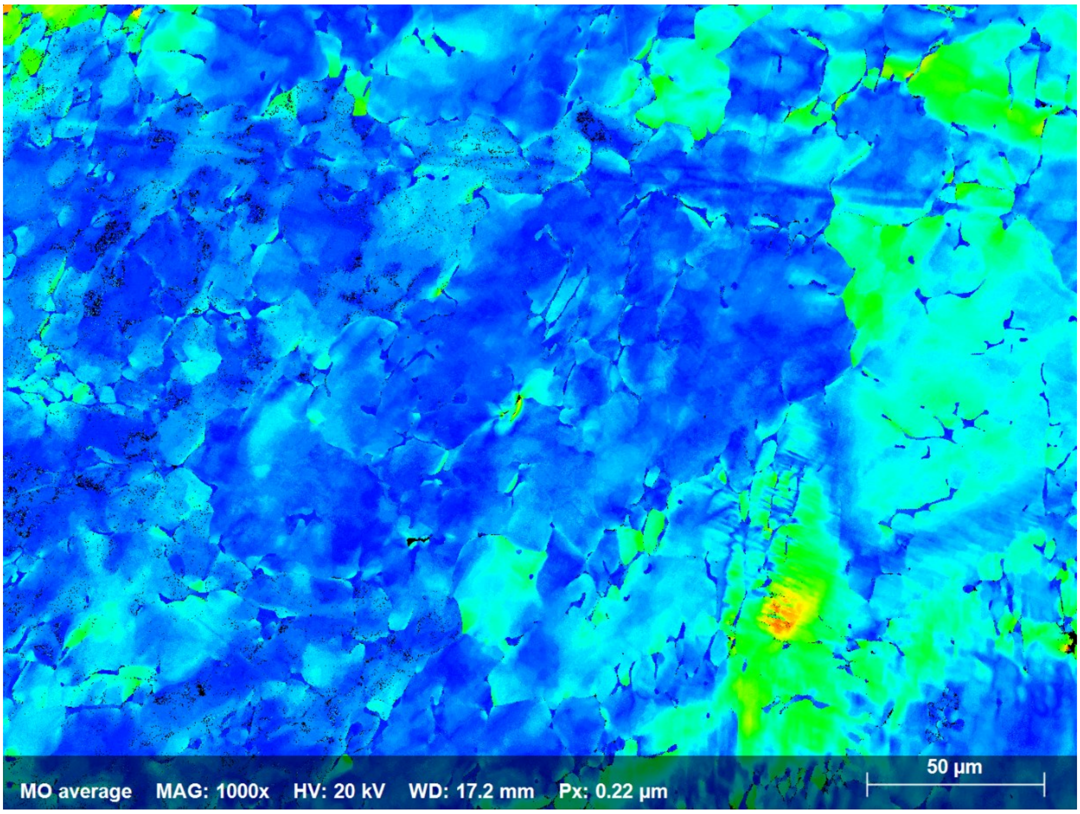

Figure 44 : MO average maps for weld metal. The map shows the yellow and green highlighted areas which shows the average misorientations within the grains while the blue areas correspond to low average misorientations.

The MO average map shown in the above figure is taken from the weld area of the type 316L SS sample. The MO average map is also distributed via different colors which shows the average misorientation between the grains, From the map, we can observe some yellow and green areas at the grain boundary areas. This is because the grain boundary are the high energy areas and the average misorientation angle can be the maximum in these areas.

Since this map is obtained from the weld area of the sample, the effect of welding and thermal stresses indicates high average misorientation values within some grains. The blue colored grains in the map indicate that the grains are mostly uniform in orientation with little or no strain accumulated in those regions.

We will compare the MO average obtained from the weld area to the one obtained from the base metal. Figure 45 shows the MO average map for the base material.

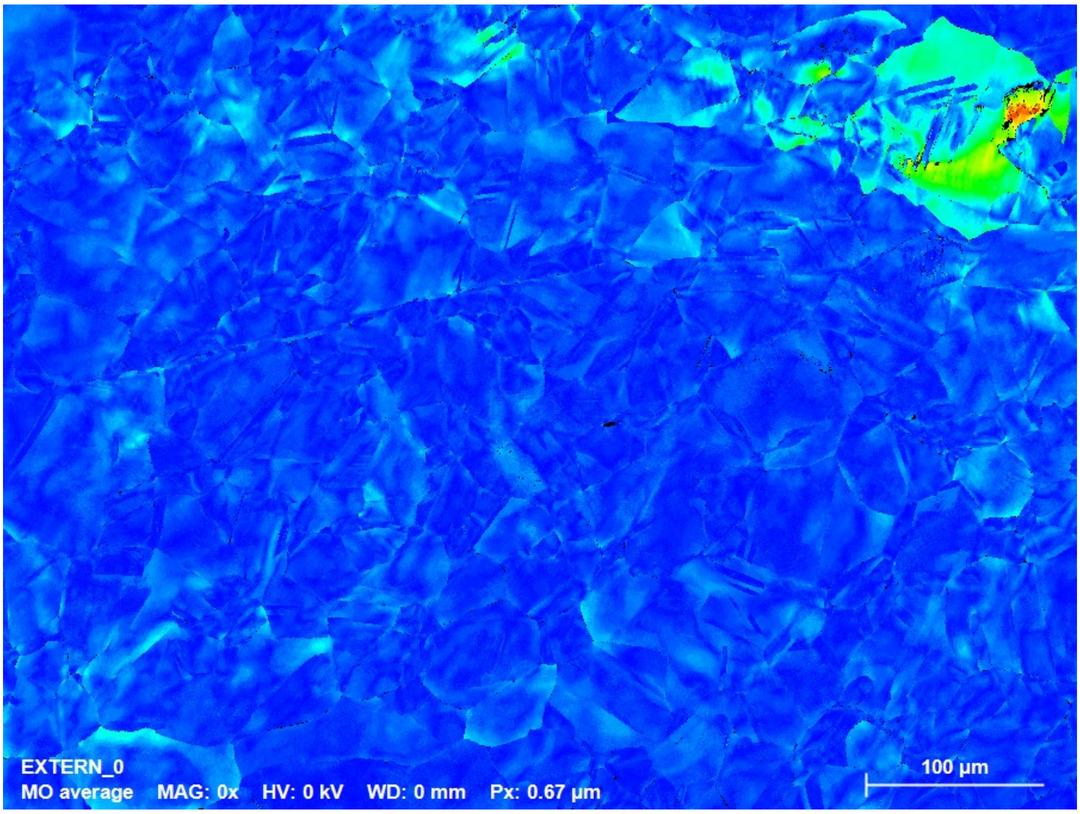

Figure 45 : MO average maps for base metal. Majority of the covered region of base metal in the image is blue indicating very little average misorientation within the grains.

The MO average map for the base material is almost filled with the blue colored grains. This indicates that the base material structure is quite uniform and there are no internal strains accumulated within the grains and at the high energy grain boundaries. The average misorientation is quite low. Although there is some yellowish area at the top right corner of the map but that could be the result of any inhomogeneities in the microstructure that could de stabilize the phase or it could be the effect of manufacturing history of the base material. Any amount of cold work in the material before welding can cause some malorientations within the grains.

# 7 Discussion

The present study investigated the potential effects of thermal loads on the SCC susceptibility of type 316L SS. The welded samples of solution annealed austenitic stainless steel (type 316L SS) under thermal cyclic loading and induced residual stresses were exposed to pressurized water reactor (PWR) environment for potential development of SCC cracks in the material. The samples showed good response to thermal cyclic loading at three different temperatures of 300,400 and 500°C and tensile residual stresses were observed. The microhardness values measured showed increased hardness values in the weld metal due to increased residual stresses resulted from thermal cyclic loading and the welding conditions.

Up to this point in the research, the results were observed as expected and in accordance with the experimental conditions in which the samples were tested. The next step involved the exposure of SS 316L samples to the PWR environment in the autoclaves in the VTT laboratory to observe any potential cracks that may have developed due to thermal cyclic loading specially in the highly thermally loaded areas which in our case was the 500°C. After keeping the samples in the autoclaves for 4 weeks, the samples were analysed for any cracks. However, contrary to our expectations, when the samples were examined under optical and electron microscopy (SEM), there were no evident cracks in the material. Electron backscattered diffraction (EBSD) analysis was carried out to monitor the deformation and misorientation within the austenitic grain structure. The EBSD results demonstrated that the grains were not equiaxed and they were asymmetrical having one dimension longer than the other. This was observed on the weld metal and the areas of thermal cyclic loading. Based on these observations, where the grain structure is not symmetric, we can predict the effect of thermal stresses and welding conditions on the weld metal. The average misorientation within the grains was also measured and the maps showed high average misorientations in the weld metal region. However, the base metal region showed very little or no average misorientation.

From the experimental results, there were few factors which were significant in defining those results. One of them can be the exposure time which was given to the thermally loaded samples in the autoclaves. The samples were kept in the high pressure autoclaves for a period of one month and this time may be is insufficient for developing any cracks on the metal surface. The samples may have required more exposure time before being examined via microscopic technique for cracks. Moreover, it was observed that the welding conditions of the pipe, the thermal loads and the resulting residual stresses were not enough to make the type 316L SS susceptible to stress corrosion cracking (SCC) when exposed to corrosive environments. There may be some third agent or extra amount of cold work required to make the material susceptible to stress corrosion cracking which in our case was not present.

# 8 Conclusion

Stress corrosion cracking has been identified as one of the most common damaging mechanisms in the nuclear industry. This type of cracking poses extreme threat as compared to conventional cracking failures to the structural integrity and safety of the nuclear power plants. Austenitic stainless steels are extensively used in the nuclear power plant components and are therefore highly susceptible to this type of failure when exposed to hight temperature and corrosive environments. Therefore, a comprehensive understanding and successful mitigation of SCC is needed to ensure the safety and integrity of the nuclear components. The aim of the present research was to investigate the potential effects of thermal loads on the SCC susceptibility of type 316L SS. The welded samples of solution annealed austenitic stainless steel (type 316L SS) under thermal cyclic loading and induced residual stresses were exposed to pressurized water reactor (PWR) environment for potential development of SCC cracks in the material. These samples when exposed to PWR environments for a particular period may develop some cracks specially in the highly thermally loaded areas. However, no evident cracks were observed after the exposure in the autoclaves. This was verified by analysing the results using optical microscopic techniques (Optical, SEM and EBSD). The findings of this study indicate that the welding conditions used for welding and the thermal cyclic loading were not enough to induce sufficient strain hardening in the material that can cause the cracks to develop once exposed to aggressive nuclear environments.

For future developments in this project, some more research needs to be conducted and the conditions need to be assessed in which austenitic stainless steels may develop some cracks when they are thermally stressed and exposed to aggressive nuclear environments. Longer exposure times and more aggressive environments may be needed to compare the results to the current study and see the difference. Repeated thermal loading on the same samples may potentially induce cumulative plastic strain and open or restart stalled SCC cracks and promote faster crack growth rate.

# References

[1] U. Ehrnstén, P. L. Andresen, and Z. Que, “A review of stress corrosion cracking of austenitic stainless steels in PWR primary water,” Jan. 01, 2024, *Elsevier B.V.* doi: 10.1016/j.jnucmat.2023.154815.

[2] “INFORMATION SHEET Detection of cracks in pipes of the emergency core cooling system of the reactors No. 1 and No. 2 of the Civaux nuclear power plant.”

[3] G. O. Ilevbare, F. Cattant, and N. K. Peat, “SCC of stainless steels under PWR service conditions,” 2011.

[4] I. Virkkunen, “Thermal Fatigue of Austenitic and Duplex Stainless Steels.”

[5] P. J. Maziasz and J. T. Busby, “2.09 - Properties of Austenitic Steels for Nuclear Reactor Applications,” in *Comprehensive Nuclear Materials: Volume 1-5*, vol. 1–5, Elsevier, 2012, pp. 267–283. doi: 10.1016/B978-0-08-056033-5.00019-7.

[6] P. J. Maziasz, “Formation and stability of radiation-induced phases in neutron-irradiated austenitic and ferritic steels,” *Journal of Nuclear Materials*, vol. 169, no. C, pp. 95–115, Dec. 1989, doi: 10.1016/0022-3115(89)90525-4.

[7] P. J. Maziasz and C. J. McHargue, “Microstructural evolution in annealed austenitic steels during neutron irradiation,” *https://doi.org/10.1179/095066087790150331*, vol. 32, no. 1, pp. 190–219, Jan. 1987, doi: 10.1179/095066087790150331.

[8] P. J. Maziasz, “Overview of microstructural evolution in neutron-irradiated austenitic stainless steels,” *Journal of Nuclear Materials*, vol. 205, no. C, pp. 118–145, Oct. 1993, doi: 10.1016/0022-3115(93)90077-C.

[9] K. Ehrlich, J. Konys, and L. Heikinheimo, “Materials for high performance light water reactors,” *Journal of Nuclear Materials*, vol. 327, no. 2–3, pp. 140–147, May 2004, doi: 10.1016/j.jnucmat.2004.01.020.

[10] J. E. Pawel, A. F. Rowcliffe, G. E. Lucas, and S. J. Zinkle, “Irradiation performance of stainless steels for ITER application l,” 1996.

[11] S. J. Zinkle, P. J. Maziasz, and R. E. Stoller, “Dose dependence of the microstructural evolution in neutron-irradiated austenitic stainless steel,” *Journal of Nuclear Materials*, vol. 206, no. 2–3, pp. 266–286, Nov. 1993, doi: 10.1016/0022-3115(93)90128-L.

[12] T. Inazumi, G. E. C. Bell, P. J. Maziasz, and T. Kondo, “Radiation-induced sensitization of a titanium-modified austenitic stainless steel irradiated in a spectral-tailored experiment at 60–400°C,” *Journal of Nuclear Materials*, vol. 191–194, no. PART B, pp. 1018–1022, Sep. 1992, doi: 10.1016/0022-3115(92)90628-X.

[13] “Overview materials issues in nuclear Reactors.” [Online]. Available: www.tms.org/jom.html

[14] U. Ehrnstén, “Environmentally-assisted cracking of stainless steels in light water reactors,” in *Nuclear Corrosion: Research, Progress and Challenges*, Elsevier, 2020, pp. 19–46. doi: 10.1016/B978-0-12-823719-9.00002-0.

[15] H. Djeloud, M. Moussaoui, R. Kouider, A. Al-Kassir, and J. P. Carrasco-Amador, “Study of the Heat Exchange and Relaxation Conditions of Residual Stresses Due to Welding of Austenitic Stainless Steel,” *Energies (Basel)*, vol. 16, no. 7, Apr. 2023, doi: 10.3390/en16073176.

[16] T.-L. Teng and C.-C. Lin, “Effect of welding conditions on residual stresses due to butt welds.”

[17] V. M. Varma Prasad, V. M. Joy Varghese, M. R. Suresh, and D. Siva Kumar, “3D Simulation of Residual Stress Developed During TIG Welding of Stainless Steel Pipes,” *Procedia Technology*, vol. 24, pp. 364–371, 2016, doi: 10.1016/j.protcy.2016.05.049.

[18] D. Deng and H. Murakawa, “Numerical simulation of temperature field and residual stress in multi-pass welds in stainless steel pipe and comparison with experimental measurements,” *Comput Mater Sci*, vol. 37, no. 3, pp. 269–277, Sep. 2006, doi: 10.1016/j.commatsci.2005.07.007.

[19] E. Borzabadi Farahani, B. Sobhani Aragh, and W. J. Mansur, “Three-dimensional finite element modelling of welding residual stresses of medium carbon steel pipes with consideration of solid-state austenite-martensite transformation and post-weld heat treatment,” *https://doi.org/10.1177/1464420719850205*, vol. 233, no. 11, pp. 2352–2364, May 2019, doi: 10.1177/1464420719850205.

[20] P. Asadi, S. Alimohammadi, O. Kohantorabi, A. Soleymani, and A. Fazli, “Numerical investigation on the effect of welding speed and heat input on the residual stress of multi-pass TIG welded stainless steel pipe,” *https://doi.org/10.1177/0954405420981335*, vol. 235, no. 6–7, pp. 1007–1021, Dec. 2020, doi: 10.1177/0954405420981335.

[21] J. J. Moverare, “Microstresses and anisotropic mechanical behaviour of duplex stainless steels,” p. 175, 2001.

[22] J. Johansson{, M. Ode Â N, and X.-H. Zeng, “EVOLUTION OF THE RESIDUAL STRESS STATE IN A DUPLEX STAINLESS STEEL DURING LOADING.”

[23] M. E. Hodson, “G.N. Eby Principles of Environmental Geochemistry. Kentucky, USA (Thomson, Brooks/Cole). 2004, 514 pp. Price £29.99 (Hardback). ISBN 0-12-229061-5,” *Mineral Mag*, vol. 67, no. 6, pp. 1321–1322, Dec. 2003, doi: 10.1180/0671321.

[24] P. Killen and A. Rafterry, “MEASUREMENTS OF RESIDUAL STRESSES IN COLD-ROLLED 304 STAINLESS STEEL PLATES USING X-RAY DIFFRACTION WITH RIETVELD REFINEMENT METHOD,” 2009.

[25] “Evaluation of changes in X-ray elastic constants and residual stress as a function of cold rolling of austenitic steels”.

[26] T. Miyazaki and T. Sasaki, “X-ray stress measurement with two-dimensional detector based on Fourier analysis,” *International Journal of Materials Research*, vol. 105, no. 9, pp. 922–927, Sep. 2014, doi: 10.3139/146.111101/MACHINEREADABLECITATION/RIS.

[27] T. Miyazaki and T. Sasaki, “X-ray residual stress measurement of austenitic stainless steel based on fourier analysis,” Apr. 01, 2016, *American Nuclear Society*. doi: 10.13182/NT15-25.

[28] X. T. Deng, M. Cheng, S. H. Zhang, H. W. Song, and M. A. Taha, “Residual stresses and martensite transformation in AISI 304 austenitic stainless steel,” *Mater Res Express*, vol. 6, no. 1, Jan. 2019, doi: 10.1088/2053-1591/aae292.

[29] A. T. Dewald, M. R. Hill, M. L. Benson, and D. L. Rudland, “MEASUREMENT OF RESIDUAL STRESS IN REACTOR NOZZLE MOCK-UPS CONTAINING DISSIMILAR METAL WELDS,” 2014. [Online]. Available: http://asmedigitalcollection.asme.org/PVP/proceedings-pdf/PVP2014/46049/V06BT06A056/4437944/v06bt06a056-pvp2014-28209.pdf

[30] J. Mathew, R. J. Moat, S. Paddea, J. A. Francis, M. E. Fitzpatrick, and P. J. Bouchard, “Through-Thickness Residual Stress Profiles in Austenitic Stainless Steel Welds: A Combined Experimental and Prediction Study,” *Metall Mater Trans A Phys Metall Mater Sci*, vol. 48, no. 12, pp. 6178–6191, Dec. 2017, doi: 10.1007/s11661-017-4359-4.

[31] T. Yonezawa, M. Watanabe, A. Hashimoto, M. D. Olson, A. T. DeWald, and M. R. Hill, “Effect of Strain Hardened Inner Surface Layers on Stress Corrosion Cracking of Type 316 Stainless Steel in Simulated PWR Primary Water,” *Metall Mater Trans A Phys Metall Mater Sci*, 2019, doi: 10.1007/s11661-019-05137-9.

[32] M. Turski and L. Edwards, “Residual stress measurement of a 316l stainless steel bead-on-plate specimen utilising the contour method,” *International Journal of Pressure Vessels and Piping*, vol. 86, no. 1, pp. 126–131, Jan. 2009, doi: 10.1016/j.ijpvp.2008.11.020.

[33] H.-J. Schindler and P. Bertschinger, “Some Steps Towards Automation of the Crack Compliance Method to Measure Residual Stress Distributions.”

[34] M. B. Prime, “Residual Stress Measurement by Successive Extension of a Slot: The Crack Compliance Method,” *Appl Mech Rev*, vol. 52, no. 2, pp. 75–96, Feb. 1999, doi: 10.1115/1.3098926.

[35] F. Hosseinzadeh, M. B. Toparli, and P. J. Bouchard, “Slitting and contour method residual stress measurements in an edge welded beam,” *Journal of Pressure Vessel Technology, Transactions of the ASME*, vol. 134, no. 1, 2012, doi: 10.1115/1.4004626.

[36] M. D. Olson, M. R. Hill, B. Clausen, M. Steinzig, and T. M. Holden, “Residual Stress Measurements in Dissimilar Weld Metal,” *Exp Mech*, vol. 55, no. 6, pp. 1093–1103, Jul. 2015, doi: 10.1007/s11340-015-0010-8.

[37] "Stress Variations Effect on the Accuracy of Slitting Method for Measuring Residual Stresses," *International Journal of Engineering*, vol. 28, no. 9 (C), 2015, doi: 10.5829/idosi.ije.2015.28.09c.15.

[38] G. S. Schajer, "Measurement of Non-Uniform Residual Stresses Using the Hole-Drilling Method. Part I-Stress Calculation Procedures," 1988. [Online]. Available: http://www.asme.or

[39] X. Li *et al.*, "Research progress of residual stress measurement methods," *Heliyon*, vol. 10, no. 7, p. e28348, Apr. 2024, doi: 10.1016/j.heliyon.2024.e28348.

[40] "Soete, W., and R. Vancrombrugge. "An industrial method... - Google Scholar." Accessed: Apr. 09, 2024. [Online]. Available: https://scholar.google.com/scholar?hl=en&as_sdt=0%2C5&q=Soete%2C+W.%2C+and+R.+Vancrombrugge.+%22An+industrial+method+for+the+determination+of+residual+stresses.%22+Proc.+SESA+8.1+%281950%29%3A+17-28.&btnG=

[41] R. A. Kelsey, "MEASURING NON-UNIFORM RESIDUAL STRESSES BY THE HOLE DRILLING METHOD."

[42] R. G. BATHGATE, "MEASUREMENT OF NON-UNIFORM BI-AXIAL RESIDUAL STRESSES BY THE HOLE DRILLING METHOD," *Strain*, vol. 4, no. 2, pp. 20–29, Apr. 1968, doi: 10.1111/J.1475-1305.1968.TB01353.X.

[43] G. S. Schajer, "Application of Finite Element Calculations to Residual Stress Measurements," *J Eng Mater Technol*, vol. 103, no. 2, pp. 157–163, Apr. 1981, doi: 10.1115/1.3224988.

[44] A. Niku-Lari, J. Lu, and J. F. Flavenot, "Measurement of residual-stress distribution by the incremental hole-drilling method," *Journal of Mechanical Working Technology*, vol. 11, no. 2, pp. 167–188, May 1985, doi: 10.1016/0378-3804(85)90023-3.

[45] M. T. Flaman, B. E. Mills, and J. M. Boag, "ANALYSIS OF STRESS-VARIATION-WITH-DEPTH MEASUREMENT PROCEDURES FOR THE RESIDUAL STRESS MEASUREMENT CENTER-HOLE METHOD OF RESIDUAL STRESS MEASUREMENT," *Exp Tech*, vol. 11, no. 6, pp. 35–37, Jun. 1987, doi: 10.1111/J.1747-1567.1987.TB00422.X.

[46] "Bijak-Zochowski, M., "A Semidestructrve Method of... - Google Scholar." Accessed: Apr. 09, 2024. [Online]. Available: https://scholar.google.com/scholar?hl=en&as_sdt=0%2C5&q=Bijak-Zochowski%2C+M.%2C+%22A+Semidestructrve+Method+of+Measuring+Residual+Stresses%2C%22+VDI-Berichte%2C+Vol.+313%2C+1978%2C+pp.+469-476.&btnG=

[47] M. T. Flaman and B. H. Manning, "Determination of residual-stress variation with depth by the hole-drilling method," *Experimental Mechanics 1985 25:3*, vol. 25, no. 3, pp. 205–207, Sep. 1985, doi: 10.1007/BF02325088.

[48] S. Suzuki *et al.*, “Stress Corrosion Cracking in Low Carbon Stainless Steel Components in BWRs,” 2009.

[49] D. Tice, “Contribution of research to the understanding and mitigation of environmentally assisted cracking in structural components of light water reactors,” *Corrosion Engineering Science and Technology*, vol. 53, no. 1, pp. 11–25, Jan. 2018, doi: 10.1080/1478422X.2017.1362158.

[50] C. F. P. N. Ilvebare G, “Assessment of cold work effects in stress corrosion cracking of stainless steels ,” Colorado Springs, Jun. 2010.

[51] “Quantification of yield strength effects on IGSCC of austenitic stainless steels in high temperature waters | Request PDF.” Accessed: Apr. 08, 2024. [Online]. Available: https://www.researchgate.net/publication/285796304_Quantification_of_yield_strength_effects_on_IGSCC_of_austenitic_stainless_steels_in_high_temperature_waters

[52] S. Nouraei, D. R. Tice, K. J. Mottershead, and D. M. Wright, “Effects of thermo-mechanical treatments on deformation behavior and IGSCC susceptibility of stainless steels in PWR primary water chemistry,” *15th International Conference on Environmental Degradation of Materials in Nuclear Power Systems-Water Reactors 2011*, vol. 3, pp. 2250–2270, 2011, doi: 10.1007/978-3-319-48760-1_144/COVER.

[53] M. Canadian Nuclear Society (CNS) and B. C. ) International Conference on Environmental Degradation of Materials in Nuclear Power Plants (13th : 2007 : Whistler, “Crack growth testing of cold worked stainless steel in a simulated PWR primary water environment to assess susceptibility to stress corrosion cracking,” 2007.

[54] “Environment1987”.

[55] T. Nolan *et al.*, “Effect of Sulfur on the SCC and Corrosion Fatigue Performance of Stainless Steel,” 2014. [Online]. Available: https://www.researchgate.net/publication/265722989

[56] “(12) United States Patent,” 2004.

[57] P. L. Andresen and F. P. Ford, “Life Prediction by Mechanistic Modeling and System Monitoring of Environmental Cracking of Iron and Nickel Alloys in Aqueous Systems*.”

[58] O. Ancelet, S. Chapuliot, G. Henaff, and S. Marie, “Development of a test for the analysis of the harmfulness of a 3D thermal fatigue loading in tubes,” *Int J Fatigue*, vol. 29, no. 3, pp. 549–564, Mar. 2007, doi: 10.1016/j.ijfatigue.2006.04.002.

[59] Y. Wang, A. Charbal, F. Hild, S. Roux, and L. Vincent, “Crack initiation and propagation under thermal fatigue of austenitic stainless steel,” *Int J Fatigue*, vol. 124, pp. 149–166, Jul. 2019, doi: 10.1016/j.ijfatigue.2019.02.036.

[60] C. Gardin, H. N. Le, G. Benoit, and D. Bertheau, “Crack growth under thermal cyclic loading in a 304L stainless steel - Experimental investigation and

numerical prediction," *Int J Fatigue*, vol. 32, no. 10, pp. 1650–1657, Oct. 2010, doi: 10.1016/j.ijfatigue.2010.03.009.

[61] E. Paffumi, K. F. Nilsson, and Z. Szaraz, "Experimental and numerical assessment of thermal fatigue in 316 austenitic steel pipes," *Eng Fail Anal*, vol. 47, no. PB, pp. 312–327, Jan. 2015, doi: 10.1016/j.engfailanal.2014.01.010.

[62] C. Robertson, M. C. Fivel, and A. Fissolo, "Dislocation substructure in 316L stainless steel under thermal fatigue up to 650 K," 2001. [Online]. Available: www.elsevier.com/locate/msea

[63] V. Maillot, A. Fissolo, G. Degallaix, and S. Degallaix, "Thermal fatigue crack networks parameters and stability: An experimental study," in *International Journal of Solids and Structures*, Jan. 2005, pp. 759–769. doi: 10.1016/j.ijsolstr.2004.06.032.

[64] A. Fissolo, B. Marini, G. Nais, and P. Wident, "Thermal fatigue behaviour for a 3 16 L type steel," 1996.

[65] Y. Lejeail and N. Kasahara, "Thermal fatigue evaluation of cylinders and plates subjected to fluid temperature fluctuations," *Int J Fatigue*, vol. 27, no. 7, pp. 768–772, Jul. 2005, doi: 10.1016/j.ijfatigue.2005.01.007.

[66] Z. H. Li, Y. M. Han, Y. G. Zhao, S. L. Yang, Z. M. Zhong, and Y. H. Lu, "Thermal corrosion fatigue crack growth behavior and life prediction of 304SS pipeline structures in high temperature pressurized water," *Eng Fail Anal*, vol. 160, Jun. 2024, doi: 10.1016/j.engfailanal.2024.108224.

[67] T. Seppänen, J. Alhainen, E. Arilahti, J. Solin, R. Vanninen, and E. Pulkkinen, "PVP2022-84007 EPR PIPING MATERIAL STUDY: BASIC CHARACTERIZATION AND LOW CYCLE FATIGUE AT ROOM TEMPERATURE."